The conserved transcriptional regulator CdnL is required for metabolic homeostasis and morphogenesis in *Caulobacter*

Selamawit Abi Woldemeskel[1], Laura Alvarez[2], Allison K. Daitch[1], Rilee Zeinert[3], Anant Bhargava[1], Diego Gonzalez[4], Justine Collier[4], Peter Chien[3], Felipe Cava[2], Erin D. Goley[1]

1: Department of Biological Chemistry, Johns Hopkins University School of Medicine, Baltimore, MD, USA
2: Department of Molecular Biology, Umeå University, Umeå, Sweden
3: Department of Biochemistry and Molecular Biology, University of Massachusetts-Amherst, MA, USA
4: Department of Fundamental Microbiology, Faculty of Biology and Medicine, University of Lausanne, Switzerland

Abstract

Bacterial growth and division require regulated synthesis of the macromolecules used to expand and replicate components of the cell. Transcription of housekeeping genes required for metabolic homeostasis and cell proliferation is guided by the sigma factor σ^{70}. The conserved CarD-like transcriptional regulator, CdnL, associates with promoter regions where σ^{70} localizes and stabilizes the open promoter complex. However, the contributions of CdnL to metabolic homeostasis and bacterial physiology are not well understood. Here, we show that *Caulobacter crescentus* cells lacking CdnL have severe morphological and growth defects. Specifically, Δ*cdnL* cells grow slowly in both rich and defined media, and are wider, more curved, and have shorter stalks than WT cells. These defects arise from transcriptional downregulation of most major classes of biosynthetic genes. Notably, we find that Δ*cdnL* cells are severely limited in glutamate synthesis, rendering them auxotrophic for that amino acid. Moreover, Δ*cdnL* cells produce low amounts of the cell wall precursor lipid II, and Δ*cdnL* is synthetic lethal with other genetic perturbations that limit lipid II production. Δ*cdnL* cells also have aberrant localization of MreB and CtpS, cytoskeletal proteins required for maintaining proper cell width and curvature. Interestingly, the localization of CtpS is dependent on availability of CTP, which is predicted to be low in Δ*cdnL* cells. Our findings implicate CdnL as a global regulator of genes required for metabolic homeostasis that impacts morphogenesis through availability of lipid II and through metabolite-mediated changes in localization of cytoskeletal regulators of cell shape.

36 **Main** (400 words)

37 In order to replicate, bacterial cells must synthesize enough macromolecules to double in
38 size using nutrients available in their environment. These macromolecules are used to build
39 structural components of the cell such as the membrane and cell wall, to synthesize the multitude
40 of enzymes required for essential biochemical processes, and to duplicate genetic material.
41 Transcriptional control of housekeeping genes encoding factors that carry out these essential
42 functions contributes to maintaining metabolic homeostasis to support growth and development.
43 Transcription initiation of housekeeping genes is achieved by housekeeping sigma factors that
44 direct the core RNA polymerase (RNAP) to their promoter regions[1], but may be co-regulated by
45 other factors, including the CarD-like transcriptional regulator CdnL. CdnL is broadly conserved
46 in bacteria and is best-characterized in *Myxococcus xanthus* and in *Mycobacteria*[2–6]. It localizes
47 to promoter regions where the housekeeping sigma factor resides, directly binds to the RNAP β
48 subunit, stabilizes the open promoter complex, and is required for transcription from rRNA
49 promoters[2,3,5]. *Mycobacterium tuberculosis* CarD (the CdnL homolog) is essential for growth in
50 culture, persistence in mice, and survival during genotoxic stress and starvation[2,4]. CdnL is also
51 essential in *M. xanthus*, where its depletion causes cell filamentation[6]. This last observation
52 implies that CdnL-dependent changes in gene expression are required to support proper
53 morphogenesis, at least in *M. xanthus*.

54 Bacterial morphology is maintained by the peptidoglycan (PG) cell wall, which must be
55 expanded and remodeled in a regulated manner to allow for growth and division. It lies just
56 outside the inner membrane and is a continuous, covalently-linked structure made of glycan
57 strands crosslinked together by peptide side chains[7]. In addition to giving the cell its stereotyped
58 shape, the cell wall provides physical integrity and prevents cell lysis due to turgor pressure.

59 Different shape features (e.g. cell length, width, or curvature) are specified by spatially and
60 temporally regulated synthesis and remodeling of the PG that is largely orchestrated by
61 cytoskeletal proteins[7,8]. Though the details of PG synthesis and remodeling and their regulation
62 by cytoskeletal proteins has been the subject of intense study for several decades, how PG
63 metabolism is regulated in coordination with nutrient availability and the metabolic status of the
64 cell is incompletely understood.

65 Here, we investigate how CdnL affects metabolism, growth, and morphogenesis in the α-
66 proteobacterium *Caulobacter crescentus* (hereafter *Caulobacter*). *Caulobacter* undergoes
67 stereotyped morphological transitions as it progresses through the cell cycle and during
68 adaptation to a variety of stresses, making it an ideal organism to study bacterial morphogenesis[9].
69 Although it is known that *Caulobacter* CdnL is not required for viability, the consequences of its
70 loss on *Caulobacter* physiology have not been previously characterized[10]. Here, we demonstrate
71 that CdnL regulates transcription of biosynthetic genes required for metabolic homeostasis that,
72 in turn, supports proper growth, PG metabolism, and morphology in *Caulobacter*.
73

74 **Results**

75 Δ*cdnL* cells have growth and morphology defects

76 We became interested in *Caulobacter* CdnL through a screen for spontaneous suppressors of a
77 dominant lethal mutant of the cell division protein FtsZ (called FtsZΔCTL) that causes lethal
78 defects in PG metabolism[11]. Specifically, one of the FtsZΔCTL suppressors we identified carried
79 a point mutation in *cdnL* (*CCNA_00690*) encoding an I42N missense mutation that disrupted
80 CdnL protein stability (Supplementary figure 1a). To examine the role of CdnL in *Caulobacter*
81 growth and morphogenesis, we deleted it in a clean genetic background and compared growth
82 and morphology to wild type (WT) cells. We found that Δ*cdnL* cells grew more slowly than WT
83 (Figure 1a) and had pleiotropic morphological defects in complex PYE medium (Figure 1b, c).
84 Quantitative analysis of shape differences between WT and Δ*cdnL* cells grown in PYE using
85 CellTool[12] revealed significant differences in two shape modes which approximately correspond
86 to cell curvature (shape mode 2) and cell width (shape mode 3) (Figure 1c). Specifically, we
87 observed that in PYE, Δ*cdnL* cells were wider and more curved than WT cells (Figure 1b, c, d).
88 In these shape modes, Δ*cdnL* cells were also more variable in their range of values than WT,
89 indicating less precise maintenance of shape in the mutant (Figure 1c). Additionally, we
90 observed phase-light "ghost" cells in Δ*cdnL* samples indicative of cell lysis and suggesting a lack
91 of integrity in the cell envelope (Figure 1b, arrows).

92 To further characterize the Δ*cdnL* growth and morphology phenotypes, we grew WT and
93 Δ*cdnL* cells in the defined media M2G or HIGG. Surprisingly, we found that M2G was unable to
94 support growth of cells lacking CdnL, but that Δ*cdnL* cells grew in HIGG, albeit more slowly
95 than WT (Figure 1a). A comparison of the components of M2G and HIGG media suggested that
96 the missing nutrient in M2G that is required for growth of Δ*cdnL* cells might be glutamate.

97 Consistent with this, addition of sodium glutamate to M2G (called M2GG with sodium
98 glutamate added) supported growth of Δ*cdnL* cells at a rate similar to that in HIGG. These data
99 indicate that Δ*cdnL* cells are unable to synthesize sufficient glutamate to support growth and are
100 now glutamate auxotrophs (Figure 1a). No other amino acids are included in either M2G or
101 HIGG, suggesting a specific requirement for exogenous glutamate.
102 Similar to our observations with PYE, we found that Δ*cdnL* cells grew more slowly than
103 WT in M2GG or HIGG and also had aberrant shape (Figure 1a, b). Δ*cdnL* cells were again
104 hypercurved and wider than WT cells, but unlike in PYE, Δ*cdnL* cells were also consistently
105 shorter than WT in each defined medium (Figure 1b, c, d). The polar stalk is a prominent
106 morphological feature of *Caulobacter* cells and, like other features of cell shape, stalk biogenesis
107 and elongation require PG synthesis[13]. Since we observed stereotyped shape changes in cells
108 lacking CdnL, we also compared stalk morphogenesis between WT and Δ*cdnL* cells. We found
109 that in phosphate replete HIGG media (containing 200 μM PO_4^-), Δ*cdnL* cells had short stalks
110 compared to WT cells (Figure 1e, f), suggesting that CdnL impacts all aspects of morphogenesis
111 in *Caulobacter*. Stalks elongate in response to phosphate starvation in *Caulobacter* through a
112 pathway that is distinct from developmentally regulated stalk morphogenesis. Interestingly,
113 Δ*cdnL* cells significantly elongated their stalks during phosphate starvation (Figure 1 e, f)
114 suggesting that Δ*cdnL* cells can still alter their morphology in response to phosphate starvation.
115
116 <u>Genes involved in biosynthetic processes are downregulated in Δ*cdnL*</u>
117 Having established that the transcriptional regulator CdnL plays a role in growth and
118 morphogenesis, we next sought to understand how it exerts these effects. To identify genes that
119 are misregulated in Δ*cdnL* that may be responsible for the growth and morphology defects that

120 we observe, we extracted mRNA from WT and Δ*cdnL* cells and performed RNA-seq. The results
121 from this analysis showed that approximately 30% of the transcriptome is misregulated in cells
122 lacking CdnL (Supplementary table 1). A closer look at genes that are downregulated in the
123 Δ*cdnL* clone that we used for RNA-seq analysis suggested that a 50 kbp region comprising 51
124 genes between CCNA_02773 and CCNA_02826 was highly downregulated in Δ*cdnL*. This
125 region is flanked by identical sequences that encode transposases CCNA_02772 and
126 CCNA_02828, suggesting that this region may be deleted in the Δ*cdnL* clone (EG1415) used in
127 our RNA-seq analysis. Indeed, deletion of this region was confirmed by PCR. However, we
128 found no differences in growth or morphology between the Δ*cdnL* clone with the 50 kbp deletion
129 (EG1415, Δ50kbp) and Δ*cdnL* clones containing this region (e.g. EG1447), indicating that this
130 region does not contribute significantly to the growth and shape defects that we observe
131 (Supplementary figure 1b, c). Previously, this region of the chromosome was shown to be readily
132 lost in a background lacking the methyltransferase *ccrM*[14]. Similar to our observations with
133 Δ*cdnL*, loss of this region in Δ*ccrM* did not yield any specific growth advantages. To ensure that
134 loss of this region did not impact our analysis of the transcriptional consequences specific to loss
135 of CdnL, we analyzed the transcriptome of an independent Δ*cdnL* clone that has the 50 kbp
136 region intact (JC784) by microarray analysis (Supplementary table 1). We found significant
137 overlap between our RNA-seq dataset using EG1415 and microarray dataset using JC784
138 (Supplementary figure 1d, e, f, g). We generally used the intersection of our two datasets (RNA-
139 seq of EG1415 and microarray of JC874) as a conservative and rigorous representation of the
140 consequences of deleting *cdnL* on the *Caulobacter* transcriptome.

141 To obtain an overview of how loss of CdnL affects the transcriptome we used DAVID[15]
142 functional annotation analysis to functionally categorize genes that had at least a two-fold change

143 in transcript abundance in Δ*cdnL* in both the RNA-seq and microarray datasets. Of the genes that
144 are downregulated in Δ*cdnL*, we found an overrepresentation of genes involved in biosynthetic
145 and bioenergetic pathways including amino acid, nucleotide, fatty acid, lipid, cell wall, cell
146 membrane, and central carbon metabolism (Supplementary table 2). Genes that are over 2-fold
147 upregulated in Δ*cdnL* clustered into categories involved in transcription, transport, and motility.
148
149 Δ*cdnL* cells have low levels of the cell wall precursor and changes in cell wall crosslinking
150 Since our transcriptome analysis revealed downregulation of pathways involved in
151 macromolecular biosynthesis, we hypothesized that the severe defects in growth and morphology
152 may arise from limited amounts of substrates available for proliferative processes. Consistent
153 with our observations that Δ*cdnL* cells are unable to grow without exogenous glutamate, we
154 found that *gdhA* and *gltB*, genes essential for glutamate biosynthesis from α-ketoglutarate or
155 glutamine, are over 4-fold downregulated in both datasets (Figure 2a). Additionally, our findings
156 from the transcriptomic analysis indicated that genes required for PG precursor (lipid II)
157 biosynthesis are highly downregulated (Figure 2a) leading us to postulate that PG material may
158 be limiting in Δ*cdnL* cells. Since PG synthesis underlies both cell shape and cell envelope
159 integrity, changes in abundance of lipid II might underlie the shape and cell lysis phenotypes
160 observed for Δ*cdnL* cells. We directly compared lipid II levels in WT and Δ*cdnL* cells and found
161 that Δ*cdnL* cells have a striking 45% reduction in lipid II levels as compared to WT (Figure 2b).
162 To assess if CdnL-mediated changes in transcription result in alterations to PG metabolic
163 activities in addition to lipid II synthesis, we performed muropeptide analysis on PG isolated
164 from WT and Δ*cdnL* cells to identify changes in PG chemistry. Consistent with low levels of
165 lipid II, Δ*cdnL* cells have 23% less PG polymer than WT (Figure 2c). Although overall PG

166 crosslinking is unaffected, Δ*cdnL* cells had significantly more dimers and fewer trimers (higher
167 order crosslinks) than WT (Figure 2d, Supplementary Figure 2b). The mutant also shows an
168 increased chain length, as the relative amount of anhydro muropeptides (glycan chain termini)
169 were significantly reduced in Δ*cdnL* cells (Figure 2e, Supplementary Figure 2b). Moreover,
170 Δ*cdnL* cells had more pentapeptides and glycine-containing muropepetides compared to WT
171 (Figure 2e, Supplementary Figure 2b). Thus, the shape and envelope integrity defects observed
172 in Δ*cdnL* cells may arise, at least in part, from a combination of low levels of lipid II and
173 significant changes in the chemical structure of the cell wall.
174
175 Pathways impacting PG metabolism become essential in Δ*cdnL*
176 To gain insight into which transcriptional changes in Δ*cdnL* may be most relevant to fitness, we
177 performed comparative transposon sequencing (Tn-Seq) on WT and Δ*cdnL* strains. Consistent
178 with morphological defects and low amounts of lipid II observed for Δ*cdnL* cells, we found
179 several normally non-essential genes involved in pathways that interact with PG synthesis that
180 could not be disrupted in the Δ*cdnL* background (Figure 3a, Supplementary table 3).
181 Specifically, we identified genes involved in glutamate metabolism, PG metabolism, PG
182 recycling, and capsule synthesis that could not be disrupted in the Δ*cdnL* background (Figure
183 3a,b, Supplementary table 3). Of the genes involved in glutamate metabolism, *gdhZ* and *murI*
184 become essential in Δ*cdnL*. Each of these proteins link glutamate metabolism to morphogenesis:
185 MurI by making D-Glu for lipid II synthesis and GdhZ via its effects on the morphogenetic
186 protein FtsZ[16,17].
187 Our Tn-Seq analysis also indicated that *ampG* and *ampD* (*CCNA_02650*), genes required
188 for PG recycling, become essential in Δ*cdnL* (Figure 3b, Supplementary table 3). AmpG is a

189 permease that allows transport of cell wall material from the periplasm to the cytoplasm, and
190 AmpD degrades transported cell wall material to provide building blocks for lipid II synthesis[18].
191 We attempted to delete *cdnL* in a Δ*ampG* backgroundf but were unable to obtain clones with
192 deletions in both *ampG* and *cdnL*, supporting the genetic interaction suggested from the Tn-Seq.
193 Since lipid II levels are low in Δ*cdnL*, the cell apparently relies on pathways that allow for
194 recycling of the existing cell wall material for survival.

195 In addition to PG metabolic genes, we found putative synthetic lethal interactions
196 between capsule (exopolysaccharide) biosynthetic genes and *cdnL* (Figure 3a,b, Supplementary
197 table 3). During capsule synthesis, saccharide precursors are synthesized on the lipid anchor
198 undecaprenyl phosphate (Und-P) in the cytoplasm, flipped to the periplasmic space, and
199 assembled into a polysaccharide that is exported to the outer surface of the cell[19]. Thus, PG
200 synthesis and capsule biosynthesis both use Und-P as a lipid carrier for synthesis and export into
201 the periplasmic space. Previous work in *Escherichia coli* and *Bacillus subtilis* has shown that
202 disruption of pathways that use Und-P can lead to Und-P sequestration and cause severe growth
203 and morphological defects by inhibiting lipid II synthesis[20–22]. Similarly, we propose that
204 disrupting the capsule biosynthesis pathway in *Caulobacter* may sequester Und-P in dead-end
205 intermediates, limiting lipid II synthesis. We attempted to delete each of the capsule genes
206 predicted by Tn-Seq to genetically interact with *cdnL* in Δ*cdnL* cells. We were unsuccessful with
207 the exception of *CCNA_00164*, which encodes a putative O-antigen polymerase ligase and which
208 had the weakest predicted genetic interaction with *cdnL* of the capsule genes (Figure 3a, b and
209 Supplementary table 3). Nevertheless, deletion of both *cdnL* and *CCNA_00164* resulted in cells
210 with morphological defects that are more severe than Δ*cdnL* alone (Figure 3d). Moreover, these
211 double mutant cells grew more slowly than Δ*cdnL* (Figure 3c). Deletion of *CCNA_00164* by

212 itself had no obvious effect on growth or morphology. Our data support the model that mutations
213 in the capsule biosynthesis pathway sequester Und-P and limit its availability for lipid II
214 synthesis, exacerbating the existing lipid II deficiency of Δ*cdnL* cells to a lethal level.
215 Collectively, our transcriptomics, biochemical analyses, and genetic interaction results indicate
216 that CdnL is required to maintain adequate availability of the PG precursor lipid II to support
217 normal growth and morphology.
218
219 MreB is hyperfocused at midcell in Δ*cdnL* cells
220 Limitation of lipid II levels has previously been shown to cause an increase in cell width in
221 *Caulobacter*[23,24]. However, the morphological defects that we observe in Δ*cdnL* cells are distinct
222 from shape changes that occur when lipid II levels are low, suggesting additional players in the
223 shape defects of Δ*cdnL* cells. To investigate this possibility, we explored other proteins
224 implicated in shape regulation in *Caulobacter*, with a focus on the polymerizing proteins MreB,
225 FtsZ, crescentin, and CTP synthase. Since CdnL is a transcriptional regulator, we first probed for
226 changes in levels of these factors and found no differences in protein or transcript levels between
227 Δ*cdnL* and WT cells (Supplementary table 2 and data not shown).
228 Since Δ*cdnL* cells had significant differences in width and curvature, we focused on the
229 cytoskeletal proteins that determine these shape features. In bacteria, the actin homolog and
230 ATPase MreB is required for rod shape, width maintenance, and cell body elongation[25,26].
231 Additionally, MreB influences curvature of *Caulobacter* cells through its effects on the
232 intermediate filament-like protein, crescentin[27]. To determine if the localization of MreB is
233 altered in Δ*cdnL*, we expressed *venus-mreB* from the *xylX* promoter and visualized MreB
234 localization in WT or Δ*cdnL* cells grown in PYE, M2G, and HIGG media (Figure 4 a,b,c). In

235 WT cells grown in PYE, MreB has a patchy localization along the length of the cell in newborn
236 swarmer (G1) cells, shifts to midcell in stalked (S) and early predivisional cells, and assumes a
237 patchy localization in late predivisional cells[25]. Interestingly, we found that the localization of
238 MreB at midcell is more tightly focused in Δ*cdnL* cells compared to WT in all three media tested
239 (Figure 4a,b,c). Moreover, we found that most WT cells localize MreB along the length of the
240 cell when grown in HIGG media (Figure 4c). However, the localization of MreB in HIGG shifts
241 to mostly at midcell when *cdnL* is deleted. To better visualize the localization of MreB across
242 populations and throughout the cell cycle, we created demographs. In cells that have MreB
243 localized at midcell, we found that the localization of MreB is more tightly focused with minimal
244 signal outside of the midcell region (Figure 4d,e,f). To quantitatively compare the differences in
245 MreB localization between WT and Δ*cdnL*, we fit the MreB signal at midcell to an eight term
246 Fourier series model and calculated the full width at half max (FWHM). We found that the
247 FWHM at midcell is smaller in Δ*cdnL* cells compared to WT, consistent with what we inferred
248 from the images and demographs (Figure 4g,h,i).

249 To further characterize the link between MreB localization and loss of *cdnL,* we deleted
250 *cdnL* in backgrounds that have mutations near the ATP binding pocket of MreB. These
251 mutations cause MreB to localize at the poles, along the length of the cell, or at midcell
252 throughout the cell cycle[27]. These aberrant localizations of MreB cause changes in cell shape but
253 do not affect growth rate (Supplementary figure 3a,b,c). Deletion of *cdnL* in each of these
254 backgrounds caused severe morphological and growth defects (Supplementary figure 3a,b). The
255 severity of growth and shape defects was worse in mutant backgrounds that do not localize MreB
256 to midcell (Supplementary figure 3). Interestingly, we found that MreB V324A, which has a
257 patchy localization in a WT background, becomes enriched at midcell when *cdnL* is deleted and

258 grows similarly to mutants that localize MreB to midcell (Supplementary figure 3b,c,d,e). These
259 data suggest that localization of MreB at midcell is important for fitness in Δ*cdnL* cells. Since
260 MreB is essential for specification and maintenance of width and curvature, the mislocalization
261 of MreB may contribute to the width and curvature defects that we observe in Δ*cdnL* cells.
262 Since we found that Δ*cdnL* cells have low lipid II levels compared to WT and lipid II has
263 been linked to localization of MreB in *B. subtilis*[28], we wanted to determine if inhibiting lipid II
264 synthesis in *Caulobacter* cells was sufficient to cause mislocalization of MreB similar to Δ*cdnL*.
265 To test this, we inhibited MurA with a low dose of fosfomycin and visualized the localization of
266 Venus-MreB over time. We observed an increase in FWHM of midcell-localized MreB and cell
267 width after 5.5 hours of fosfomycin treatment (Supplementary Figure 4a,b,c). The changes in
268 localization of MreB during fosfomycin treatment are opposite to what we observe during *cdnL*
269 deletion, suggesting other mechanisms by which MreB is enriched at midcell in Δ*cdnL* cells.
270
271 <u>Hypercurvature of Δ*cdnL* cells is dependent on crescentin and may involve CTP synthase</u>
272 In *Caulobacter*, crescentin drives the patterning of PG synthesis required for cell curvature[8,29].
273 To determine if hypercurvature of Δ*cdnL* cells is dependent on crescentin, we deleted *cdnL* in a
274 Δ*creS* background. We observed that Δ*cdnL*Δ*creS* cells are straight, indicating that
275 hypercurvature is dependent on crescentin (Figure 5a,b). In addition to crescentin, curvature is
276 influenced by the metabolic enzyme CTP synthase (CtpS), which forms filaments near crescentin
277 when CTP is abundant[30,31]. CtpS filaments negatively regulate curvature in a crescentin-
278 dependent manner[31]. Since we observed that pyrimidine biosynthetic genes are downregulated
279 from our RNA-Seq analysis (Figure 5c), we hypothesized that the hypercurvature of Δ*cdnL* may
280 arise due to fewer CtpS filaments caused by low levels of CTP in Δ*cdnL*. To gain support for this

281 hypothesis, we expressed *mcherry-ctpS* from the xylose promoter in WT or Δ*cdnL* cells and
282 visualized its localization (Supplementary figure 5). Demograph analysis of mCherry-CtpS
283 localization indicated that mCherry-CtpS forms less robust filaments and has more dispersed
284 signal in Δ*cdnL* cells grown in PYE or M2GG compared to WT (Figure 5d, Supplementary
285 figure 5). Our data support the hypothesis that low levels of CTP in Δ*cdnL* cells lead to
286 formation of fewer CtpS filaments than in WT, which consequently yields the hypercurvature we
287 observe.
288
289

290 Discussion

291 In this work, we unveil a new role for the conserved global transcriptional regulator
292 CdnL in mediating transcription of biosynthetic genes required for metabolic homeostasis in
293 *Caulobacter*. We show that in Δ*cdnL* cells, transcription of many classes of biosynthetic genes is
294 downregulated, with physiologically critical defects in glutamate and lipid II metabolism in
295 particular. These changes in metabolic pools affect growth and morphology directly by limiting
296 macromolecules required for envelope expansion and indirectly by influencing morphogenetic
297 proteins. Downregulation of genes involved in biosynthetic and bioenergetics pathways in Δ*cdnL*
298 cells and the reliance of Δ*cdnL* cells on exogenous glutamate, which is a central node in multiple
299 biosynthetic pathways, suggests that CdnL is a global regulator of genes required for central
300 metabolism and macromolecular synthesis[32,33].

301 Previously, CdnL has been shown to directly bind to RNAP and stabilize the open
302 promoter complex required for transcription of rRNA promoters in *Mycobacteria* and *M.*
303 *xanthus*[3,5]. Similarly, *Caulobacter* CdnL has been shown to bind RNAP and regulate
304 transcription from an rRNA promoter[10]. Here, we demonstrate that loss of CdnL has global
305 effects on various aspects of bacterial metabolism. Interestingly, however, transcriptomic
306 changes that occur during loss of CdnL in *Caulobacter* are the opposite of what is observed in
307 *Mycobacterium smegmatis*. CarD depletion in *M. smegmatis* leads to upregulation of genes
308 encoding the translation machinery and enzymes in metabolic pathways, such as amino acid
309 biosynthesis, and to downregulation of genes involved in degradation of amino acids, fatty acid
310 metabolism and those coding for membrane proteins[2]. Although loss of CdnL generally has
311 opposite effects on expression of metabolic genes in these two divergent bacteria, CdnL-

312 mediated effects on the transcriptome impact proliferative and metabolic processes and are
313 thereby essential for proper growth in *Caulobacter* and viability in *Mycobacteria*.
314 In *Caulobacter*, loss of CdnL causes aberrant morphogenesis, at least in part, by limiting
315 production of lipid II. The effects of *cdnL* deletion are in some ways reminiscent of loss of the
316 master regulator and RNA chaperone Hfq in *Caulobacter*[23]. Deletion of *hfq* alters the levels of
317 several metabolites, including glutamate and components of the TCA cycle. Importantly, this
318 includes accumulation of α-oxoglutarate which, in turn, causes reduced synthesis of lipid II and
319 pleiotropic cell shape defects[23]. Though both Hfq and CdnL are required to maintain sufficiently
320 high levels of lipid II to support growth and stereotyped cell shape, CdnL has a distinct shape
321 phenotype, likely mediated by additional impacts on MreB and CtpS.
322 In recent years, a growing number of factors have been described that link the metabolic
323 status of the cell to morphology through cytoskeletal proteins [7,33,34]. The best-studied examples
324 of this employ moonlighting functions of metabolic enzymes to couple metabolism to
325 morphology. For example, the glucosyltransferases UgtP and OpgH in *B. subtilis* and *E. coli,*
326 respectively, alter FtsZ dynamics and affect cell size in a UDP-glucose dependent manner[35,36].
327 Similarly, in *Caulobacter*, GdhZ and KidO alter FtsZ assembly in a glutamate-dependent
328 manner, coupling metabolism to cell division[16,37]. In the case of CdnL, its impact on the
329 localization of the cytoskeletal proteins MreB and CtpS appears to be metabolite-mediated rather
330 than protein-mediated. Polymerization of CtpS into filaments that negatively regulate cell
331 curvature is dependent on CTP, which is predicted to be present in low amounts in Δ*cdnL* cells.
332 It is unclear how MreB localization is regulated in *Caulobacter*, though it appears to be linked to
333 its ATP-dependent polymerization cycle[27] and may involve cell wall precursors other than lipid
334 II. Thus, we propose that the disruption of metabolic homeostasis that arises from loss of CdnL

335 impacts morphology through metabolite-mediated effects on cytoskeletal proteins in addition to
336 reduced levels of lipid II.

337 Interestingly, depletion of CdnL in *M. xanthus* results in cell filamentation, consistent
338 with a conserved impact on morphogenesis[6]. The effects, if any, of CarD depletion in
339 *Mycobacteria* on cell morphology have not been reported, nor have the effects of CdnL depletion
340 on the *M. xanthus* transcriptome or metabolome. Future work in diverse organisms will reveal if
341 the role of CdnL as a global regulator of both morphogenesis and metabolism is conserved
342 across bacteria.

343
344

345 Methods

346 **Bacterial strains, plasmids, growth conditions**

347 *Caulobacter crescentus* NA1000 strains were grown in peptone yeast extract medium (PYE),
348 M2G[38], M2GG (M2G with 0.15% sodium glutamate), or Hutner base imidazole-buffered glucose
349 glutamate medium (HIGG)[39]. Xylose was used at 0.3% for induction experiments. EG1415 and
350 JC874 were used for RNA-Seq and microarray experiments, respectively. All other experiments
351 with Δ*cdnL* were performed using EG1447 (clean, in-frame deletion of *cdnL*) or EG1898 (*cdnL*
352 coding sequence replaced with *aacC1,* conferring gentamicin resistance) or derivatives thereof.
353 JC874, EG1447, and EG1898 contain the 50 kbp region that is deleted in EG1415. Growth
354 curves were performed in a Tecan Infinite M200 Pro plate reader, 100 µL culture volume, with
355 the OD_{600} of each strain monitored in biological triplicates every 30 min with intermittent
356 shaking. Antibiotics for growing *Caulobacter* and cloning and purifying plasmids from *E. coli*
357 were used at concentrations in liquid (solid) media as described in Woldemeskel *et al* 2017[40]. *C.*
358 *crescentus*: kanamycin 5 (25) µg/mL, gentamicin 1 (5) µg/mL. *E. coli:* ampicillin 50 (100)
359 µg/mL, kanamycin 30 (50) µg/mL, gentamicin 15 (20) µg/mL, and spectinomycin 50 (50)
360 µg/mL.

361 **Phase contrast, ensemble fluorescence microscopy and image analysis**

362 Cells in exponential phase of growth were spotted on 1% agarose pads and imaged using a Nikon
363 Eclipse Ti inverted microscope equipped with a Nikon Plan Fluor 100X (NA1.30) oil Ph3
364 objective and Photometrics CoolSNAP HQ^2 cooled CCD camera. Chroma filter cubes ET-EYFP
365 and ET-dsRED were used for Venus and mCherry, respectively. Images were processed using
366 Adobe Photoshop and demographs were made using Oufti[41]. Principal component analysis to
367 identify shape variations were performed using CellTool[12] after phase contrast images were

368 converted to binary masks in ImageJ[42] and edited in Adobe Photoshop to remove overlapping
369 cells. Full-width at half-maximum (FWHM) calculations of midcell MreB signal from Oufti[41]
370 output were performed using a custom MATLAB script which fit the normalized signal output
371 from Oufti[41] into an eighth term Fourier series model. Cells for which the fit had an adjusted R
372 square value greater than 0.85 were chosen for FWHM calculation. Cells that have midcell
373 localized MreB were selected for FWHM determination based on cell length bins guided by
374 demographs.

375 **Immunoblotting to assess CdnL levels**

376 His_6-SUMO-CdnL was overproduced in Rosetta (DE3) pLysS *E.coli* cells from pEG1129 by
377 inducing for 3 hr at 30 ^oC with 0.5 mM IPTG at OD_{600} of 0.5. Cells were harvested by
378 centrifugation, resuspended in lysis buffer (50 mM Tris-HCl, pH 8.0, 300 mM KCl, 20 mM
379 imidazole, and 10% glycerol), lysed with 1 mg/mL lysozyme, sonicated and centrifuged at 4 ^oC
380 for 30 min at 15000 x g. Supernatant was loaded onto a HisTrap FF 1 mL column (GE Life
381 Sciences) and eluted with lysis buffer with 300 mM imidazole, cleaved with His_6-Ulp1 (SUMO
382 protease) at 1:500 (protease: fusion) molar ratio overnight while dialyzing into lysis buffer.
383 Sample was reloaded onto HisTrap FF 1mL and flow through collected to separate His_6-SUMO
384 and His_6-Ulp1 from CdnL. CdnL fraction was dialyzed into PBS prior to antibody production.
385 Cells in log phase were isolated and lysed in SDS-PAGE loading buffer by boiling for 5 min.
386 Standard procedures were used for SDS-PAGE and transfer to nitrocellulose membrane. CdnL
387 antisera was generated by immunizing a rabbit with CdnL purified as above (Pocono Rabbit
388 Farm & Laboratory). Specificity was determined using cell lysates with deleted or overexpressed
389 *cdnL*. CdnL antisera was used at 1:5000.

390 **RNA-Seq preparation**

391 Cultures of three independent colonies of WT (EG865) and Δ*cdnL* (EG1415, Δ50kbp) cells were
392 grown in PYE and harvested at OD_{600} of 0.45 and total RNA was extracted using PureLink RNA
393 Mini Kit from Thermo Fisher using the protocol provided with the kit. Briefly, cells were
394 harvested, lysed, and homogenized using lysozyme, SDS, provided Lysis buffer, and
395 homogenizer. Nucleic acids were extracted with ethanol and loaded onto the provided spin
396 cartridge. DNA-free total RNA was extracted using the on-column PureLink DNAse Treatment
397 protocol. PureLink DNAse mixture was directly added on to the spin cartridge membrane,
398 incubated for 15 min and washed using provided wash buffers and RNA was eluted with
399 RNAse-free water. Finally, RNA quality was quantified using a bioanalyzer and rRNA was
400 removed using the Ribo-Zero rRNA Removal Kit (Gram-Negative Bacteria). RNA-Seq libraries
401 were prepared using the Illumina TruSeq stranded RNA kit and sequenced on an Illumina HiSeq
402 2500. Data analysis was performed using the Illumina's CASAVA 1.8.2, Bowtie2 (v 2.2.5), and
403 Bioconductor's DESeq package. rRNA clean up, quality control analysis, library prep,
404 sequencing and analysis was performed by the Johns Hopkins University School of Medicine
405 Next Generation Sequencing Center.

406 **Microarray preparations**

407 Biological triplicates of WT (JC450) and Δ*cdnL* (JC784) cultures grown in PYE were harvested
408 at OD_{660} of 0.3. RNA was extracted with Trizol, purified using Ambion PureLink RNA mini-kit
409 according to manufacturer's protocol. Double stranded cDNA was prepared with Roche Double
410 Stranded cDNA synthesis kit. Microarray analysis was performed on Nimblegen custom chips
411 following the manufacturer's protocol for labeling, hybridization on 4-plex chips, and washing.
412 Scanning was performed with Agilent microarray scanner at 3 μm and normalization was
413 performed with Nimblescan implemented RMA algorithm (3 x 4-plex chips in total, all samples

414 from the same culture conditions). The statistical analysis of significance was performed with R
415 using the Significance of Analysis of Microarrays (SAM) method implemented in the library
416 *siggenes.*[43]

417 **DAVID analysis and functional clustering**

418 Genes with a two-fold change in transcript levels in both RNA-Seq and microarray analysis were
419 functionally categorized using DAVID[15] with a medium classification stringency and default
420 parameters.

421 **Transposon library preparation, sequencing, and analysis**

422 Two Tn-Seq libraries each were generated for WT (EG865) and Δ*cdnL* (EG1447). 1L PYE
423 cultures were harvested at OD_{600} of 0.4-0.6, washed 5 times with 10% glycerol, and
424 electroporated with the Ez-Tn5 <Kan-2> transposome (Epicentre). Cells were recovered for 90
425 minutes at 30 ^{o}C with shaking, and plated on PYE-Kan plates. WT libraries were grown for 5
426 and 6 days and Δ*cdnL* libraries were grown for 6 and 10 days. Colonies were scraped off plates,
427 combined, resuspended to form a homogeneous solution in PYE, and flash frozen in 20%
428 glycerol. Genomic DNA for each library was extracted from an aliquot using the DNeasy Blood
429 and Tissue Kit (Qiagen). Libraries were then prepared for Illumina Next-Generation sequencing
430 through sequential PCR reactions. The first PCR round used arbitrary hexamer primers with a
431 Tn5 specific primer going outward. The second round used indexing primers with unique
432 identifiers to filter artifacts arising from PCR duplicates. Indexed libraries were pooled and
433 sequenced at the University of Massachusetts Amherst Genomics Core Facility on the NextSeq
434 550 (Illumina).

435 Sequencing reads were first demultiplexed by index, each library was concatenated and clipped
436 of the molecular modifier added in the second PCR using Je[44]:

437 java -jar /je_1.2/je_1.2_bundle.jar clip F1=compiled.gz LEN=6

438 Reads were then mapped back to the *Caulobacter crescentus* NA1000 genome (NCBI Reference

439 Sequence: NC_011916.1) using BWA[45] and sorted using Samtools[46]:

440 bwa mem -t2 clipped.gz | samtools sort -@2 - > sorted.bam

441 Duplicates were removed using Je[44] and indexed with Samtools[46] using the following command:

442 java -jar /je_1.2/je_1.2_bundle.jar markdupes I=sorted.bam O=marked.bam M=METRICS.txt

443 MM=0 REMOVE_DUPLICATES=TRUE

444 samtools index marked.bam

445 The 5' insertion site of each transposon were converted into .wig files comprising of counts per

446 position and visualized using Integrative Genomics Viewer (IGV)[47,48]. Specific hits for each

447 library were determined with coverage and insertion frequency using a bedfile containing all

448 open reading frames from NC_011916.1 and the outer 20% of each removed to yield a clean and

449 thorough insertion profile. This was determined using BEDTools[49,50] and the following

450 commands:

451 bedtools genomecov -5 -bg marked.bam > marked.bed

452 bedtools map -a NA1000.txt -b marked.bed -c 4 > output.txt

453 Library comparisons were performed using the edgeR package in the Bioconductor suite using a

454 quasi-likelihood F-test (glmQLFit) to determine the false discovery rate adjusted p-values

455 reported here.

456 **Lipid II extraction and analysis**

457 Precursor extraction was performed as described previously and performed in triplicates[28].

458 Briefly, 500 mL of WT and Δ*cdnL* were grown in PYE to OD_{600} of 0.45. Cells were harvested,

459 resuspended in 5 mL PBS and poured into 50 mL flasks containing 20 mL $CHCl_3$:Methanol

460 (1:2). The mixture was stirred for 1 h at room temperature and centrifuged for 10 min at 4000 x g
461 at 4 ºC. The supernatant was transferred to clean 250 mL flasks containing 12 mL $CHCl_3$ and 9
462 mL PBS, stirred for 1 h at room temperature and centrifuged for 10 min at 4000 x g at 4 ºC. The
463 interface fraction (between the top aqueous and bottom organic layers) was collected and
464 vacuum dried. To remove lipid tail, samples were resuspended in 100 µL DMSO and 800 µL
465 H_2O, 100 µL ammonium acetate 100 mM pH 4.2 were added. This mixture was boiled for 30
466 min, dried in vacuum and resuspended in 300 µL H_2O. Samples were analyzed by UPLC
467 chromatography coupled to MS/MS analysis, using a Xevo G2- XS QTof system (Waters
468 Corporation, USA). The separation method used is identical to the one used for muropeptide
469 separation explained below. A library of compounds was used to target the identification of
470 peptidoglycan precursors and possible intermediates, although only lipid II (lipid II-penta) was
471 detected in these samples. Lipid II amounts were calculated based on the integration of the peaks
472 (total area), normalized to the culture OD.

473 **Peptidoglycan (PG) purification and analysis**

474 PG samples were analyzed as described previously[51,52]. Briefly, 50 mL of WT and Δ*cdnL* cells
475 were grown to an OD_{600} of 0.5 in PYE, harvested, and boiled in 5% SDS for 2 h. Sacculi were
476 repeatedly washed with MilliQ water by ultracentrifugation (110,000 rpm, 10 min, 20 ºC) until
477 total removal of the detergent and finally treated with muramidase (100 µg/mL) for 16 hours at
478 37 ºC. Muramidase digestion was stopped by boiling and coagulated proteins were removed by
479 centrifugation (10 min, 14,000 rpm). For sample reduction, the pH of the supernatants was
480 adjusted to pH 8.5-9.0 with sodium borate buffer and sodium borohydride was added to a final
481 concentration of 10 mg/mL. After incubating for 30 min at room temperature, pH was adjusted
482 to 3.5 with orthophosphoric acid.

483 UPLC analyses of muropeptides were performed on a Waters UPLC system (Waters
484 Corporation, USA) equipped with an ACQUITY UPLC BEH C18 Column, 130Å, 1.7 µm, 2.1
485 mm X 150 mm (Waters, USA) and a dual wavelength absorbance detector. Elution of
486 muropeptides was detected at 204 nm. Muropeptides were separated at 45 °C using a linear
487 gradient from buffer A (formic acid 0.1% in water) to buffer B (formic acid 0.1% in acetonitrile)
488 in an 18-minute run, with a 0.25 mL/min flow. Relative total PG amounts were calculated by
489 comparison of the total intensities of the chromatograms (total area) from three biological
490 replicates normalized to the same OD_{600} and extracted with the same volumes. Muropeptide
491 identity was confirmed by MS/MS analysis, using a Xevo G2-XS QTof system (Waters
492 Corporation, USA). Quantification of muropeptides was based on their relative abundances
493 (relative area of the corresponding peak) normalized to their molar ratio.
494

495 **References**

496 1. Österberg, S., Peso-Santos, T. del & Shingler, V. Regulation of Alternative Sigma Factor
497 Use. *Annu. Rev. Microbiol.* **65**, 37–55 (2011).
498 2. Stallings, C. L. *et al.* CarD Is an Essential Regulator of rRNA Transcription Required for
499 Mycobacterium tuberculosis Persistence. *Cell* **138**, 146–159 (2009).
500 3. Srivastava, D. B. *et al.* Structure and function of CarD, an essential mycobacterial
501 transcription factor. *Proc. Natl. Acad. Sci.* **110**, 12619–12624 (2013).
502 4. Weiss, L. A. *et al.* Interaction of CarD with RNA Polymerase Mediates Mycobacterium
503 tuberculosis Viability, Rifampin Resistance, and Pathogenesis. *J. Bacteriol.* **194**, 5621–5631
504 (2012).
505 5. Gallego-García, A. *et al.* Structural Insights into RNA Polymerase Recognition and Essential
506 Function of Myxococcus xanthus CdnL. *PLOS ONE* **9**, e108946 (2014).
507 6. García-Moreno, D. *et al.* CdnL, a member of the large CarD-like family of bacterial proteins,
508 is vital for Myxococcus xanthus and differs functionally from the global transcriptional
509 regulator CarD. *Nucleic Acids Res.* **38**, 4586–4598 (2010).
510 7. Typas, A., Banzhaf, M., Gross, C. A. & Vollmer, W. From the regulation of peptidoglycan
511 synthesis to bacterial growth and morphology. *Nat. Rev. Microbiol.* **10**, 123–136 (2012).
512 8. Cabeen, M. T. *et al.* Bacterial cell curvature through mechanical control of cell growth.
513 *EMBO J.* **28**, 1208–1219 (2009).
514 9. Woldemeskel, S. A. & Goley, E. D. Shapeshifting to Survive: Shape Determination and
515 Regulation in Caulobacter crescentus. *Trends Microbiol.* **25**, 673–687 (2017).

516 10. Gallego-García, A. *et al. Caulobacter crescentus* CdnL is a non-essential RNA polymerase-
517 binding protein whose depletion impairs normal growth and rRNA transcription. *Sci. Rep.* **7**,
518 43240 (2017).
519 11. Sundararajan, K. *et al.* The bacterial tubulin FtsZ requires its intrinsically disordered linker
520 to direct robust cell wall construction. *Nat. Commun.* **6**, 7281 (2015).
521 12. Pincus, Z. & Theriot, J. A. Comparison of quantitative methods for cell-shape analysis. *J.*
522 *Microsc.* **227**, 140–156 (2007).
523 13. Seitz, L. C. & Brun, Y. V. Genetic Analysis of Mecillinam-Resistant Mutants ofCaulobacter
524 crescentus Deficient in Stalk Biosynthesis. *J. Bacteriol.* **180**, 5235–5239 (1998).
525 14. Gonzalez, D. & Collier, J. Genomic Adaptations to the Loss of a Conserved Bacterial DNA
526 Methyltransferase. *mBio* **6**, e00952-15 (2015).
527 15. Dennis, G. *et al.* DAVID: Database for Annotation, Visualization, and Integrated Discovery.
528 *Genome Biol.* **4**, P3 (2003).
529 16. Beaufay, F. *et al.* A NAD-dependent glutamate dehydrogenase coordinates metabolism with
530 cell division in Caulobacter crescentus. *EMBO J.* **34**, 1786–1800 (2015).
531 17. Doublet, P., Heijenoort, J. van, Bohin, J. P. & Mengin-Lecreulx, D. The murI gene of
532 Escherichia coli is an essential gene that encodes a glutamate racemase activity. *J. Bacteriol.*
533 **175**, 2970–2979 (1993).
534 18. Park, J. T. Why does Escherichia coli recycle its cell wall peptides? *Mol. Microbiol.* **17**, 421–
535 426 (1995).
536 19. Ardissone, S. *et al.* Cell cycle constraints on capsulation and bacteriophage susceptibility.
537 *eLife* **3**, (2014).

538 20. Jorgenson, M. A., Kannan, S., Laubacher, M. E. & Young, K. D. Dead-end intermediates in
539 the enterobacterial common antigen pathway induce morphological defects in Escherichia
540 coli by competing for undecaprenyl phosphate. *Mol. Microbiol.* **100**, 1–14 (2016).
541 21. Jorgenson, M. A. & Young, K. D. Interrupting Biosynthesis of O Antigen or the
542 Lipopolysaccharide Core Produces Morphological Defects in Escherichia coli by
543 Sequestering Undecaprenyl Phosphate. *J. Bacteriol.* **198**, 3070–3079 (2016).
544 22. D'Elia, M. A. *et al.* Probing Teichoic Acid Genetics with Bioactive Molecules Reveals New
545 Interactions among Diverse Processes in Bacterial Cell Wall Biogenesis. *Chem. Biol.* **16**,
546 548–556 (2009).
547 23. Irnov, I. *et al.* Crosstalk between the tricarboxylic acid cycle and peptidoglycan synthesis in
548 Caulobacter crescentus through the homeostatic control of α-ketoglutarate. *PLOS Genet.* **13**,
549 e1006978 (2017).
550 24. Harris, L. K. & Theriot, J. A. Relative Rates of Surface and Volume Synthesis Set Bacterial
551 Cell Size. *Cell* **165**, 1479–1492 (2016).
552 25. Figge, R. M., Divakaruni, A. V. & Gober, J. W. MreB, the cell shape-determining bacterial
553 actin homologue, co-ordinates cell wall morphogenesis in Caulobacter crescentus. *Mol.*
554 *Microbiol.* **51**, 1321–1332 (2004).
555 26. Takacs, C. N. *et al.* MreB Drives De Novo Rod Morphogenesis in Caulobacter crescentus
556 via Remodeling of the Cell Wall. *J. Bacteriol.* **192**, 1671–1684 (2010).
557 27. Dye, N. A., Pincus, Z., Fisher, I. C., Shapiro, L. & Theriot, J. A. Mutations in the nucleotide
558 binding pocket of MreB can alter cell curvature and polar morphology in Caulobacter. *Mol.*
559 *Microbiol.* **81**, 368–394 (2011).

560 28. Qiao, Y. *et al.* Lipid II overproduction allows direct assay of transpeptidase inhibition by β-
561 lactams. *Nat. Chem. Biol.* **13**, 793–798 (2017).
562 29. Ausmees, N., Kuhn, J. R. & Jacobs-Wagner, C. The Bacterial Cytoskeleton: An Intermediate
563 Filament-Like Function in Cell Shape. *Cell* **115**, 705–713 (2003).
564 30. Barry, R. M. *et al.* Large-scale filament formation inhibits the activity of CTP synthetase.
565 *eLife* **3**, (2014).
566 31. Ingerson-Mahar, M., Briegel, A., Werner, J. N., Jensen, G. J. & Gitai, Z. The metabolic
567 enzyme CTP synthase forms cytoskeletal filaments. *Nat. Cell Biol.* **12**, 739–746 (2010).
568 32. Commichau, F. M., Forchhammer, K. & Stülke, J. Regulatory links between carbon and
569 nitrogen metabolism. *Curr. Opin. Microbiol.* **9**, 167–172 (2006).
570 33. Sperber, A. M. & Herman, J. K. Metabolism Shapes the Cell. *J. Bacteriol.* **199**, e00039-17
571 (2017).
572 34. Cabeen, M. T. & Jacobs-Wagner, C. Bacterial cell shape. *Nat. Rev. Microbiol.* **3**, 601–610
573 (2005).
574 35. Hill, N. S., Buske, P. J., Shi, Y. & Levin, P. A. A Moonlighting Enzyme Links Escherichia
575 coli Cell Size with Central Metabolism. *PLOS Genet.* **9**, e1003663 (2013).
576 36. Weart, R. B. *et al.* A metabolic sensor governing cell size in bacteria. *Cell* **130**, 335–347
577 (2007).
578 37. Radhakrishnan, S. K., Pritchard, S. & Viollier, P. H. Coupling Prokaryotic Cell Fate and
579 Division Control with a Bifunctional and Oscillating Oxidoreductase Homolog. *Dev. Cell* **18**,
580 90–101 (2010).
581 38. Marks, M. E. *et al.* The Genetic Basis of Laboratory Adaptation in Caulobacter crescentus. *J.*
582 *Bacteriol.* **192**, 3678–3688 (2010).

583 39. Poindexter, J. S. Selection for Nonbuoyant Morphological Mutants of Caulobacter
584 crescentus. **135**, 5 (1978).
585 40. Woldemeskel, S. A., McQuillen, R., Hessel, A. M., Xiao, J. & Goley, E. D. A conserved
586 coiled-coil protein pair focuses the cytokinetic Z-ring in Caulobacter crescentus. *Mol.*
587 *Microbiol.* **105**, 721–740 (2017).
588 41. Paintdakhi, A. *et al.* Oufti: An integrated software package for high-accuracy, high-
589 throughput quantitative microscopy analysis. *Mol. Microbiol.* **99**, 767–777 (2016).
590 42. Schneider, C. A., Rasband, W. S. & Eliceiri, K. W. NIH Image to ImageJ: 25 years of image
591 analysis. *Nat. Methods* **9**, 671–675 (2012).
592 43. Schwender, H., Krause, A. & Ickstadt, K. Comparison of the Empirical Bayes and the
593 Significance Analysis of Microarrays. 26
594 44. Girardot, C., Scholtalbers, J., Sauer, S., Su, S.-Y. & Furlong, E. E. M. Je, a versatile suite to
595 handle multiplexed NGS libraries with unique molecular identifiers. *BMC Bioinformatics* **17**,
596 419 (2016).
597 45. Li, H. & Durbin, R. Fast and accurate long-read alignment with Burrows–Wheeler transform.
598 *Bioinformatics* **26**, 589–595 (2010).
599 46. Li, H. *et al.* The Sequence Alignment/Map format and SAMtools. *Bioinformatics* **25**, 2078–
600 2079 (2009).
601 47. Robinson, J. T. *et al.* Integrative Genomics Viewer. *Nat. Biotechnol.* **29**, 24–26 (2011).
602 48. Thorvaldsdóttir, H., Robinson, J. T. & Mesirov, J. P. Integrative Genomics Viewer (IGV):
603 high-performance genomics data visualization and exploration. *Brief. Bioinform.* **14**, 178–
604 192 (2013).

605 49. McCarthy, D. J., Chen, Y. & Smyth, G. K. Differential expression analysis of multifactor
606 RNA-Seq experiments with respect to biological variation. *Nucleic Acids Res.* **40**, 4288–
607 4297 (2012).
608 50. Robinson, M. D., McCarthy, D. J. & Smyth, G. K. edgeR: a Bioconductor package for
609 differential expression analysis of digital gene expression data. *Bioinformatics* **26**, 139–140
610 (2010).
611 51. Alvarez, L., Hernandez, S. B., de Pedro, M. A. & Cava, F. Ultra-Sensitive, High-Resolution
612 Liquid Chromatography Methods for the High-Throughput Quantitative Analysis of
613 Bacterial Cell Wall Chemistry and Structure. in *Bacterial Cell Wall Homeostasis: Methods*
614 *and Protocols* (ed. Hong, H.-J.) 11–27 (Springer New York, 2016). doi:10.1007/978-1-4939-
615 3676-2_2
616 52. Desmarais, S. M., Pedro, M. A. D., Cava, F. & Huang, K. C. Peptidoglycan at its peaks: how
617 chromatographic analyses can reveal bacterial cell wall structure and assembly. *Mol.*
618 *Microbiol.* **89**, 1–13 (2013).
619

620 **Acknowledgements**

621 We thank members of the Goley lab for helpful discussions and input. We thank Kousik
622 Sundararajan for identifying the initial mutant of CdnL that suppresses the FtsZΔCTL
623 phenotype. We would like to thank Julie Theriot, Lucy Shapiro, Christine Jacobs-Wagner, Regis
624 Hallez, and Zemer Gitai for providing materials and strains used in this project. We thank the
625 Johns Hopkins Genetic Resources Core Facility for RNA-Seq services and analysis and Zach
626 Pincus for guidance in using CellTool. This work was funded by the NIH through
627 R01GM108640 (to EDG), R01GM111706 (to PC), T32GM08515 (training grant support of RZ),
628 and T32GM007445 (training grant support of AKD) and Johns Hopkins Discovery Fund grant to
629 EDG. JC is funded by Swiss National Science Foundation (SNSF) grants 31003A_140758 and
630 31003A_173075. Research in the Cava lab is supported by MIMS, the Knut and Alice
631 Wallenberg Foundation (KAW), the Swedish Research Council, and the Kempe Foundation.

632

633

634 **Author contributions**

635 SAW and EDG conceived the study. SAW, LA, RZ, DG, JC, PC, FC, and EDG designed the
636 experiments. SAW performed the majority of experiments and analysis, except as noted. LA
637 performed muropeptide analysis and lipid II quantification. SAW, AKD, RZ, and PC performed
638 and/or analyzed Tn-Seq experiments. AB wrote custom software to analyze MreB distribution.
639 DG performed and analyzed microarray experiments. EDG purified CdnL, generated strains, and
640 performed CellTool analysis of shape. JC, PC, FC, and EDG supervised the research. SAW and
641 EDG wrote the manuscript with support and editing from all authors.

642

643 **Figure Legends**

644 **Figure 1: Cells lacking CdnL have pleiotropic morphological and growth defects. a**. Growth
645 of WT (EG865) and Δ*cdnL* (EG1447) cells in the indicated media. **b.** Phase contrast images of
646 WT and Δ*cdnL* cells grown in the indicated media. Arrows indicate ghost cells. Bar = 2 µm. **c.**
647 PCA of cell shape for WT and Δ*cdnL* shown in **b.** Scatter plots of shape modes 1, 2, and 3
648 approximately correspond to length, curvature and width. Contours on the left of scatter plots
649 indicate mean cell shape and standard deviations (s.d) from the mean. **d.** Mean shapes of WT and
650 Δ*cdnL* cells grown in the indicated media. **e.** Membrane staining of EG865 (WT) and EG1447
651 (Δ*cdnL*) cells with FM4-64 after growth in HIGG media with and without phosphate. **f.** Stalk
652 lengths measured using ImageJ's[42] line tool. Mean and SEM included for plots in **c.** and **f.**
653 Statistical analysis in **c.** and **f.** performed using one-way ANOVA with Bonferroni's Multiple
654 Comparison Test, n = 500 for each in **c.** n = 150, 127, 168, 155, 162, 172 from left to right in **e.**
655 *** = P < 0.001, * = P < 0.05, ns = not significant.

656

657 **Figure 2: CdnL impacts cell wall precursor synthesis and cell wall metabolism. a.** Heatmap
658 showing changes of the indicated transcripts involved in lipid II synthesis and cell wall
659 remodeling in WT (EG865) and Δ*cdnL* (EG1415) using RNA-Seq. **b. & c.** Relative amount of
660 lipid II and peptidoglycan in WT (EG865) and Δ*cdnL* (EG1447) cells. **d. & e.** Indicated
661 muropeptide species from WT (EG865) and Δ*cdnL* (EG1447). X-axis shown in **e.** are (1-6
662 anhydro) N-acetyl muramic acid (anhydro), Gly containing muropeptides (Gly),and
663 pentapeptides (penta). Values in **b., c., d. & e.** are from three independent cultures and mean and
664 SEM are indicated. Statistical analysis performed using unpaired t test. *** = P < 0.001, ** = P <
665 0.01, * = P < 0.05.

666

667 **Figure 3: Mutations in cell wall recycling and capsule biosynthetic genes are synthetic**

668 **lethal with Δ*cdnL*. a.** Volcano plot representation of Tn-Seq analysis. Negative $\log_{10}$ of the false

669 discovery rate (-log(FDR)) is plotted against $\log_2$ of the fold change in number of unique

670 transposon insertions in each gene in WT (EG865) vs Δ*cdnL* (EG1447). Genes that become

671 essential in the Δ*cdnL* background and are discussed in this study are color-coded. **b.** Transposon

672 insertion profile for selected genes from **a. c. & d.** Growth curves and phase contrast images for

673 WT (EG865), Δ*cdnL* (EG1447), Δ*CCNA_00164* (EG2604) and Δ*cdnL* Δ*CCNA_00164*

674 (EG2804). Bar = 2 µm.

675

676 **Figure 4: MreB localization is aberrant in Δ*cdnL* cells. a., b. & c.** Merged phase contrast

677 (blue) and fluorescence (yellow) images of WT (EG1795) and Δ*cdnL* cells (EG2465) expressing

678 *venus-mreB* for 2 hrs from the *xylX* promoter in the indicated media. Bar = 2 µm. **d., e. & f.**

679 Demographs of images shown in **a., b. &c.** n = 850 cells for each. **g., h. & i.** Scatter plots of full

680 width at half maximum (FWHM) values of midcell-localized MreB. Cell length range used for

681 FWHM calculation of midcell-localized MreB was determined from demographs shown in **d.-f.**.

682 For PYE, WT and Δ*cdnL*, cells 2 – 3 µm long have MreB localized at midcell and were selected

683 for FWHM calculations. For M2GG, WT and Δ*cdnL* cells between lengths of 3 – 3.75 µm and 2

684 – 3 µm, respectively, were selected for FWHM calculations. For HIGG, WT and Δ*cdnL* cells

685 between lengths of 3 – 3.5 µm and 2 – 3 µm, respectively, were selected for FWHM

686 calculations. Statistical analysis performed using unpaired t test. *** = $P < 0.001$. n = 140 each

687 for PYE and HIGG and n = 383 each for M2GG.

688

689 **Figure 5: Hypercurvature of Δ*cdnL* cells is dependent on crescentin and may involve CTP**
690 **synthase. a.** Phase contrast images of WT (EG865), Δ*creS* (EG1903), Δ*cdnL::gentR* (EG1898)
691 and Δ*creS* Δ*cdnL::gentR* (EG1912). **b.** Scatter plot depicting shape mode 2 (~curvature) from
692 PCA of cell shape for cells shown in **a**. Mean and SEM values are indicated. n = 447, 615, 734,
693 574 from left to right. Contours on the left of scatter plots indicate mean cell shape and standard
694 deviations (s.d) from the mean. Statistical analysis performed using one-way ANOVA with
695 Bonferroni's Multiple Comparison Test. *** = $P < 0.001$, ns = not significant. **c.** Heatmap
696 showing changes of indicated transcripts involved in pyrimidine biosynthesis in WT (EG865)
697 and Δ*cdnL* (EG1415) using RNA-Seq. **d.** Demographs of images from Supplementary Figure 4
698 of WT (EG1902) and Δ*cdnL* (EG1958) cells expressing *mCherry – ctpS* from the *xylX* locus
699 grown in indicated media. n = 400 cells for each.
700
701

Supplementary Figures Legends

Supplementary figure 1: RNA-seq and microarray analysis using strains EG1415 and JC784 have significant overlap. a. Immunoblot against whole cell lysates of the indicated strains probed with CdnL antisera. **b.** Phase contrast images and **c.** growth curves of WT (EG865), Δ*cdnL* (EG1447) and Δ*cdnL; Δ50kb* (EG1415). Bar = 2 µm. **d.** Pie chart comparing RNA-Seq data using EG1415 and microarray data using JC784. A 2-fold change in transcript level was used as the cut-off for up- or downregulation. **e.** Pearson's correlation between microarray (y – axis) and RNA-Seq (x – axis) data. Pearson r = 0.6331; significant correlation with alpha = 0.05. **f & g.** Zoomed in scatter plots depicting correlation between microarray (y – axis) and RNA-Seq (x – axis) for ≥2-fold upregulated genes **(f)** and ≥2-fold down regulated **(g)** genes in both data sets.

Supplementary figure 2: Muropeptide composition is altered in Δ*cdnL* cells. a. Representative chromatograms of the muramidase-digested sacculi of WT and Δ*cdnL* cells. **b.** Relative molar abundance (%) of monomers, dimers, trimers, percentage of crosslinkage (proportion of crosslinked peptide side chains), muropeptides with a residue of (1-6 anhydro) N-acetyl muramic acid (Anhydro), Gly containing muropeptides (Gly muropep.), and pentapeptides. **c.** Muropeptide relative molar abundance (%). GlcNAc: *N*-Acetyl glucosamine. MurNAc: *N*-Acetyl muramic acid. Ala: Alanine. Glu: Glutamic acid. mDAP: meso-diaminopimelic acid. Gly: Glycine. Statistical analysis performed using t-test analysis. * = $P < 0.05$ and > 10% variation compared to WT.

725 **Supplementary figure 3: *mreB* mutants are synthetic sick with Δ*cdnL*. a.** Phase contrast
726 images of WT and Δ*cdnL* cells expressing indicated *mreB* mutants at the *mreB* locus. Bar = 2
727 µm. **b.** Growth curves of strains shown in **(a)** grown in PYE. **c.** Summary of the localization of
728 MreB mutants from Dye et al, 2011.[27] **d.** Localization of indicated MreB mutants by expressing
729 mutant version of *venus-mreB* from *xylX* locus. **e.** Demographs of MreB mutants shown in **(d).**
730
731 **Supplementary figure 4: Depletion of lipid II by treating cells with fosfomycin causes an**
732 **increase in cell width and FWHM of MreB localization. a.** Merged images of cells expressing
733 *venus-mreB* from the *xylX* promoter and treated with fosfomycin for indicated amount of time
734 before imaging. Blue: phase contrast, yellow: Venus-MreB. Bar = 2 µm. **b.** Maximum cell width
735 of cells shown in **(a).** n = 500 each, *** = $P < 0.001$, ns = not significant using one-way ANOVA
736 with Bonferroni's Multiple Comparison Test. **c.** Full width at half maximum (FWHM) values of
737 Venus-MreB in cells between 2.5 – 3 µm long and which have MreB localized at midcell. n =
738 245, *** = $P < 0.001$, ns = not significant using one-way ANOVA with Bonferroni's Multiple
739 Comparison Test.
740
741 **Supplementary figure 5. CTP synthase localization is weak in Δ*cdnL* cells compared to WT**.
742 Phase contrast, fluorescent and merged images of WT (EG1902) and Δ*cdnL* (EG1958) cells
743 expressing *mCherry – ctpS* from the *xylX* locus grown in indicated media. Bar = 2 µm.
744
745 **Supplementary table 1**: RNA-Seq and microarray data for EG1415 and JC784, respectively.
746 Gene (CCNA), annotation, fold change in Δ*cdnL* over wild-type, $\log_2$ of fold change, and

747 statistical significance (1 = significant, 0 = not significant) are presented for each dataset. The 50
748 kb deletion in EG1415 is highlighted.
749
750 **Supplementary table 2**: DAVID[15] functional analysis of the set of genes great than or equal to
751 2-fold up-regulated or 2-fold down-regulated in both RNAseq and microarray datasets from
752 supplementary table 1. Functional annotation clusters identified, their enrichment scores, cluster
753 names, and the gene numbers for that cluster are indicated.
754
755 **Supplementary table 3**: Tn-Seq data for EG1447 (ΔcdnL) and EG865 (WT). The number of
756 unique transposon insertions in each gene in wild-type compared to Δ*cdnL* was used to
757 determine the $\log_2$ fold-change in number of unique transposon insertions (logFC), log counts
758 per million reads (logCPM), PValue, false-discovery rate (FDR), and negative $\log_{10}$ of the FDR
759 for each gene in WT versus Δ*cdnL*.
760
761 **Supplementary table 4:** Strains and plasmids used in this study.

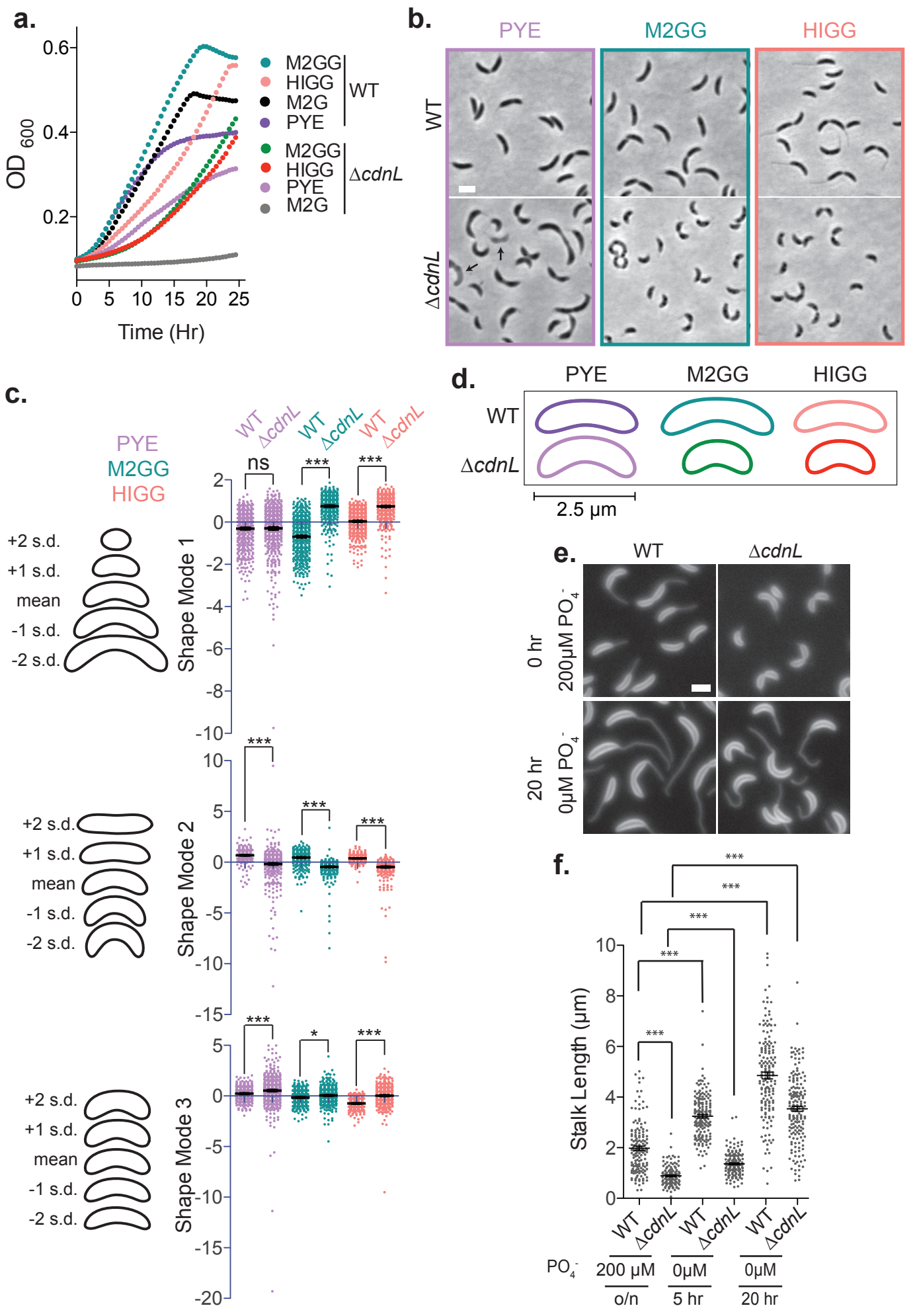

Figure 1: Cells lacking CdnL have pleiotropic morphological and growth defects. a. Growth of WT (EG865) and ΔcdnL (EG1447) cells in the indicated media. b. Phase contrast images of WT and ΔcdnL cells grown in the indicated media. Arrows indicate ghost cells. Bar = 2 µm. c. PCA of cell shape for WT and ΔcdnL shown in b. Scatter plots of shape modes 1, 2, and 3 approximately correspond to length, curvature and width. Contours on the left of scatter plots indicate mean cell shape and standard deviations (s.d) from the mean. d. Mean shapes of WT and ΔcdnL cells grown in the indicated media. e. Membrane staining of EG865 (WT) and EG1447 (ΔcdnL) cells with FM4-64 after growth in HIGG media with and without phosphate. f. Stalk lengths measured using ImageJ's42 line tool. Mean and SEM included for plots in c. and f. Statistical analysis in c. and f. performed using one-way ANOVA with Bonferroni's Multiple Comparison Test, n = 500 for each in c. n = 150, 127, 168, 155, 162, 172 from left to right in e. *** = P < 0.001, * = P < 0.05, ns = not significant.

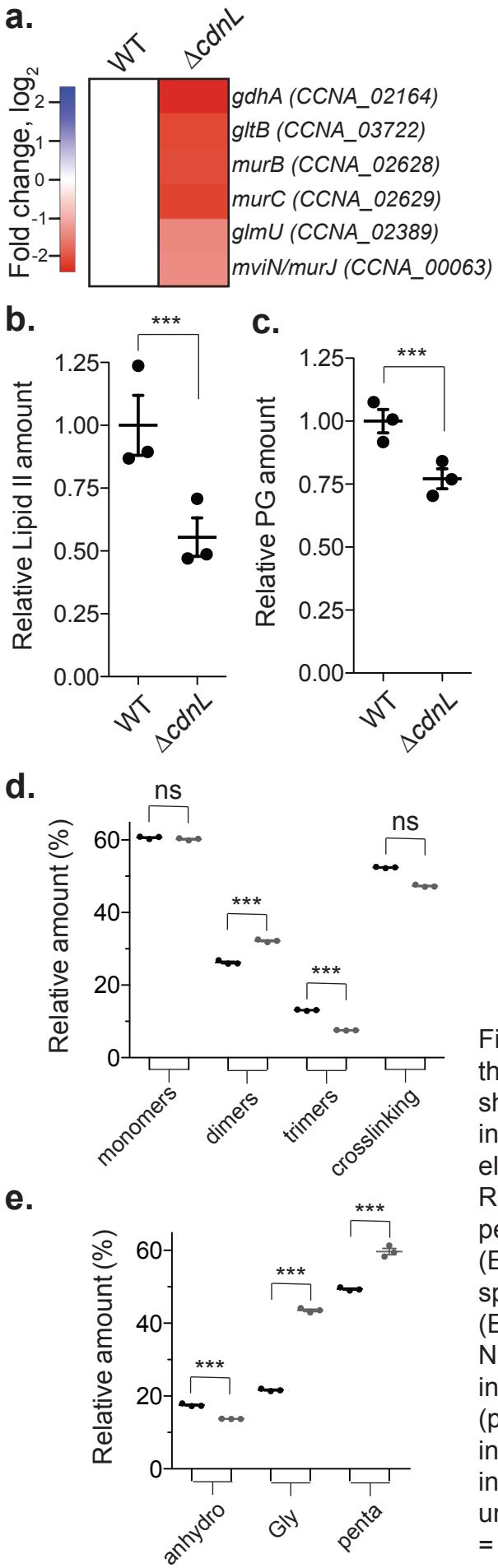

Figure 2: CdnL impacts cell wall precursor synthesis and cell wall metabolism. a. Heatmap showing changes of the indicated transcripts involved in lipid II synthesis and cell wall remodeling in WT (EG865) and ΔcdnL (EG1415) using RNA-Seq. b. & c. Relative amount of lipid II and peptidoglycan in WT (EG865) and ΔcdnL (EG1447) cells. d. & e. Indicated muropeptide species from WT (EG865) and ΔcdnL (EG1447). X-axis shown in e. are (1-6 anhydro) N-acetyl muramic acid (anhydro), Gly containing muropeptides (Gly),and pentapeptides (penta). Values in b., c., d. & e. are from three independent cultures and mean and SEM are indicated. Statistical analysis performed using unpaired t test. *** = P < 0.001, ** = P < 0.01, * = P < 0.05.

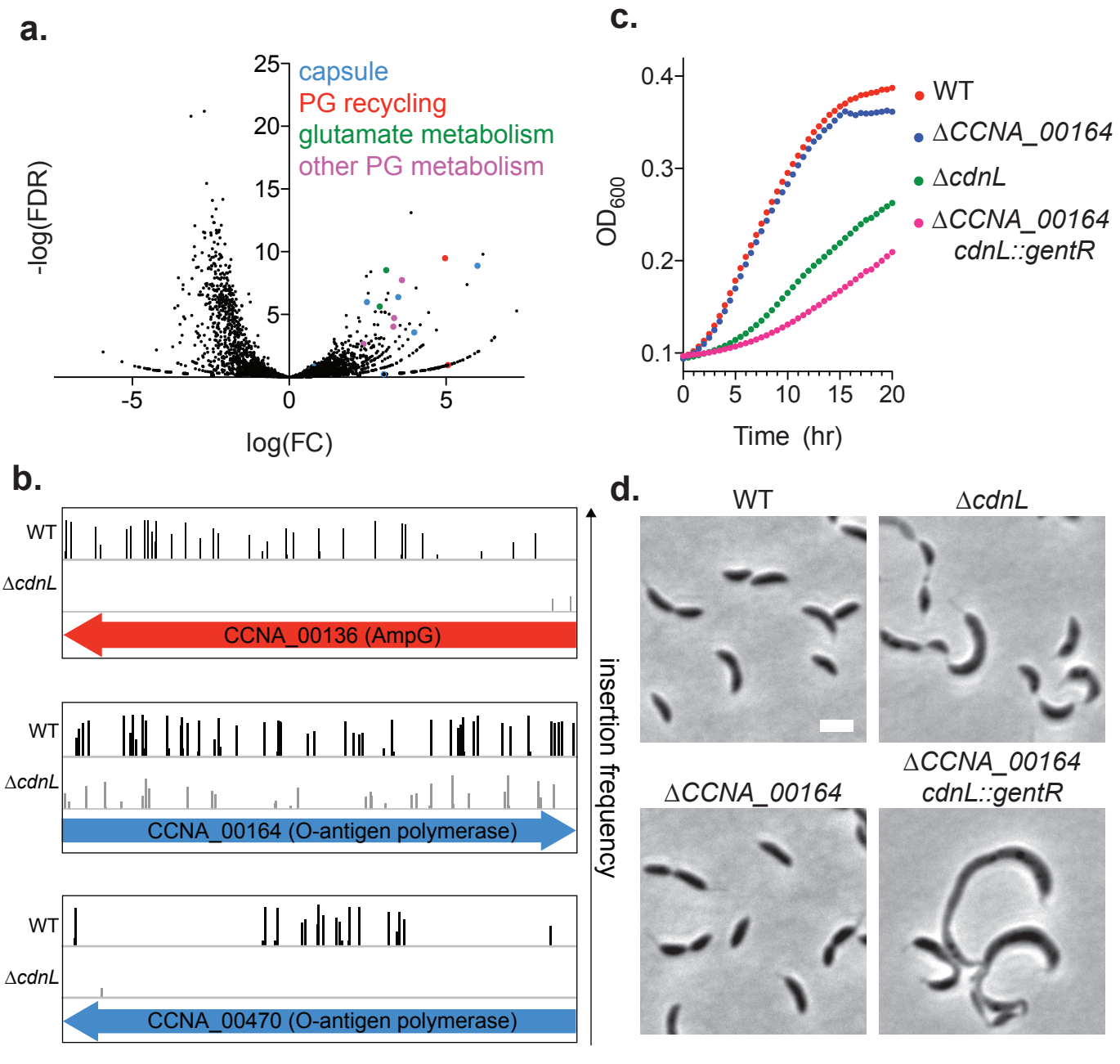

Figure 3: Mutations in cell wall recycling and capsule biosynthetic genes are synthetic lethal with ΔcdnL. a. Volcano plot representation of Tn-Seq analysis. Negative log10 of the false discovery rate (-log(FDR)) is plotted against log2 of the fold change in number of unique transposon insertions in each gene in WT (EG865) vs ΔcdnL (EG1447). Genes that become essential in the ΔcdnL background and are discussed in this study are color-coded. b. Transposon insertion profile for selected genes from a. c. & d. Growth curves and phase contrast images for WT (EG865), ΔcdnL (EG1447), ΔCCNA_00164 (EG2604) and ΔcdnL ΔCCNA_00164 (EG2804). Bar = 2 μm.

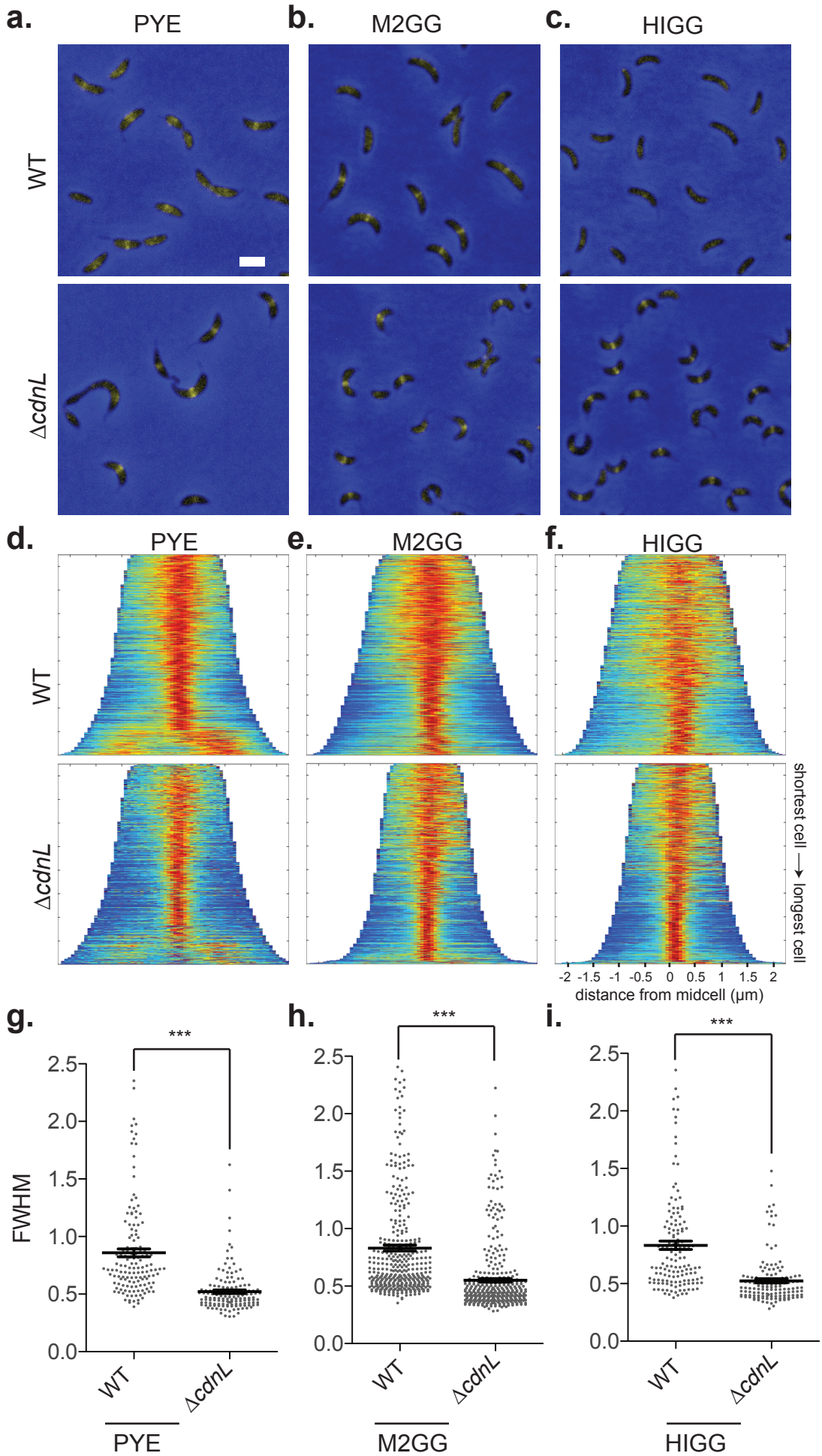

Figure 4: MreB localization is aberrant in ΔcdnL cells. a., b. & c. Merged phase contrast (blue) and fluorescence (yellow) images of WT (EG1795) and ΔcdnL cells (EG2465) expressing venus-mreB for 2 hrs from the xylX promoter in the indicated media. Bar = 2 μm. d., e. & f. Demographs of images shown in a., b. &c. n = 850 cells for each. g., h. & i. Scatter plots of full width at half maximum (FWHM) values of midcell-localized MreB. Cell length range used for FWHM calculation of midcell-localized MreB was determined from demographs shown in d.-f.. For PYE, WT and ΔcdnL, cells 2 – 3 μm long have MreB localized at midcell and were selected for FWHM calculations. For M2GG, WT and ΔcdnL cells between lengths of 3 – 3.75 μm and 2 – 3 μm, respectively, were selected for FWHM calculations. For HIGG, WT and ΔcdnL cells between lengths of 3 – 3.5 μm and 2 – 3 μm, respectively, were selected for FWHM calculations. Statistical analysis performed using unpaired t test. *** = $P < 0.001$. n = 140 each for PYE and HIGG and n = 383 each for M2GG.

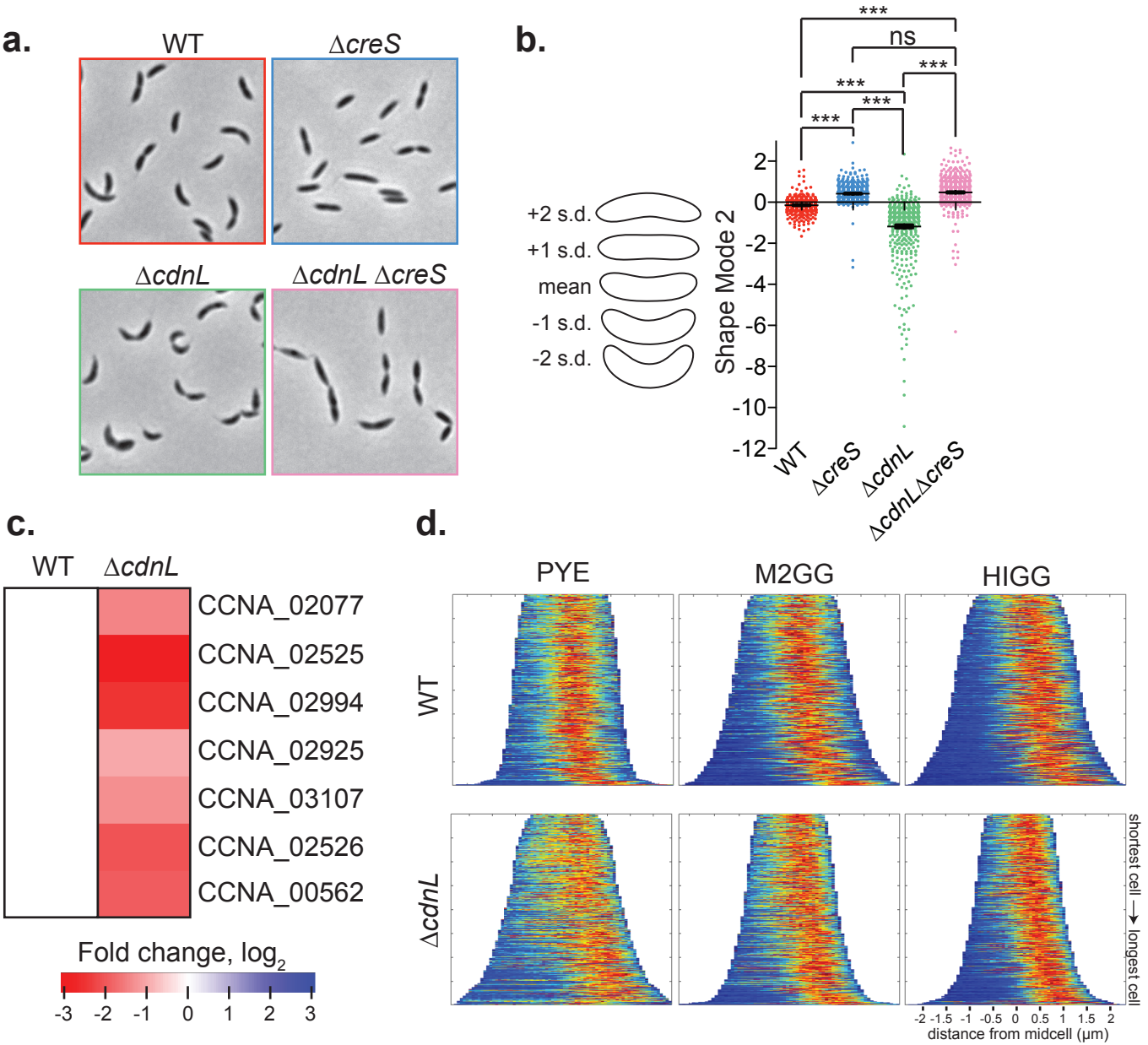

Figure 5: Hypercurvature of ΔcdnL cells is dependent on crescentin and may involve CTP synthase. a. Phase contrast images of WT (EG865), ΔcreS (EG1903), ΔcdnL::gentR (EG1898) and ΔcreS ΔcdnL::gentR (EG1912). b. Scatter plot depicting shape mode 2 (~curvature) from PCA of cell shape for cells shown in a. Mean and SEM values are indicated. n = 447, 615, 734, 574 from left to right. Contours on the left of scatter plots indicate mean cell shape and standard deviations (s.d) from the mean. Statistical analysis performed using one-way ANOVA with Bonferroni's Multiple Comparison Test. *** = P < 0.001, ns = not significant. c. Heatmap showing changes of indicated transcripts involved in pyrimidine biosynthesis in WT (EG865) and ΔcdnL (EG1415) using RNA-Seq. d. Demographs of images from Supplementary Figure 4 of WT (EG1902) and ΔcdnL (EG1958) cells expressing mCherry – ctpS from the xylX locus grown in indicated media. n = 400 cells for each.

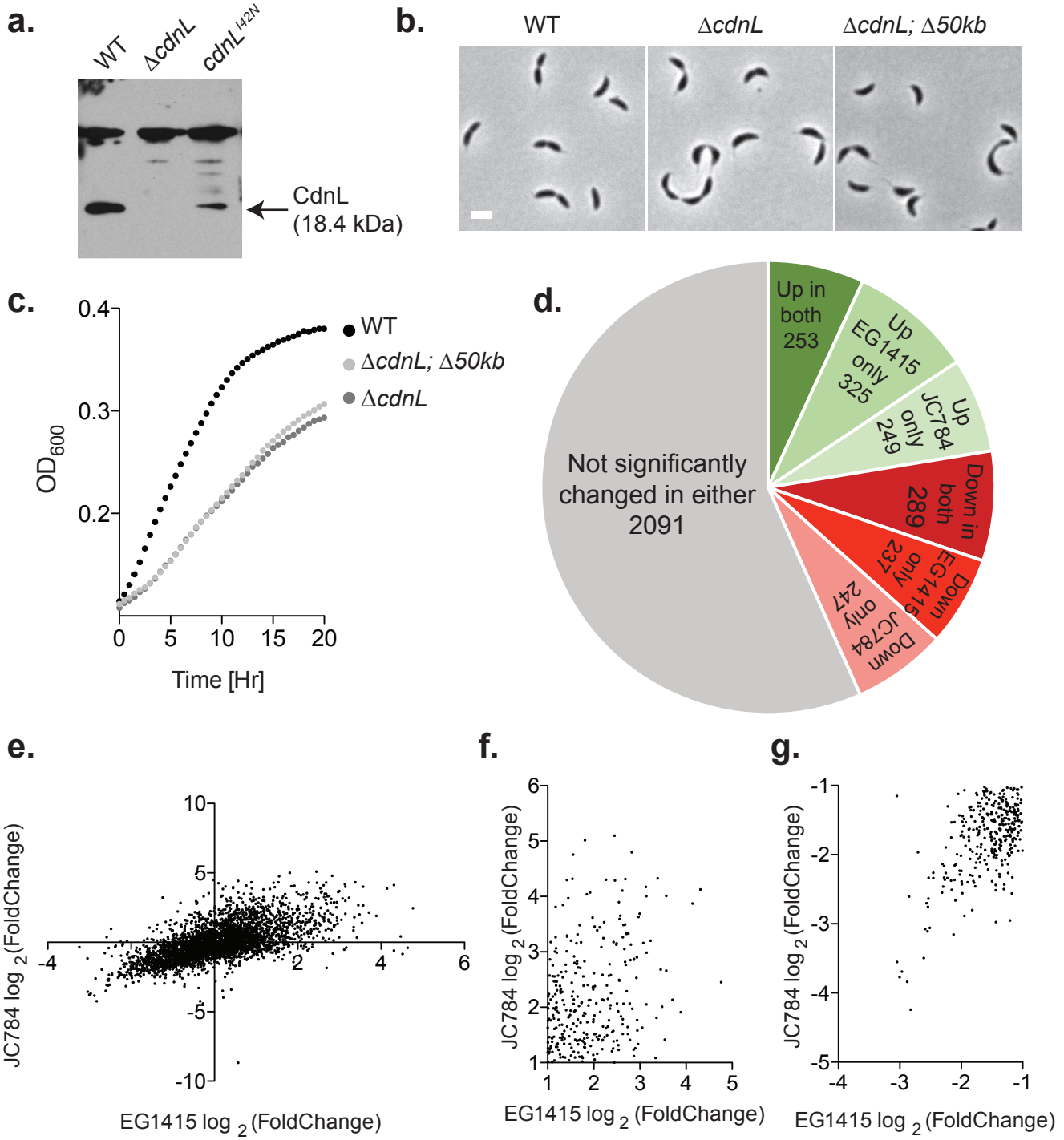

Supplementary figure 1: RNA-seq and microarray analysis using strains EG1415 and JC784 have significant overlap. a. Immunoblot against whole cell lysates of the indicated strains probed with CdnL antisera. b. Phase contrast images and c. growth curves of WT (EG865), ΔcdnL (EG1447) and ΔcdnL; Δ50kb (EG1415). Bar = 2 μm. d. Pie chart comparing RNA-Seq data using EG1415 and microarray data using JC784. A 2-fold change in transcript level was used as the cut-off for up- or downregulation. e. Pearson's correlation between microarray (y – axis) and RNA-Seq (x – axis) data. Pearson r = 0.6331; significant correlation with alpha = 0.05. f & g. Zoomed in scatter plots depicting correlation between microarray (y – axis) and RNA-Seq (x – axis) for ≥2-fold upregulated genes (f) and ≥2-fold down regulated (g) genes in both data sets.

a.

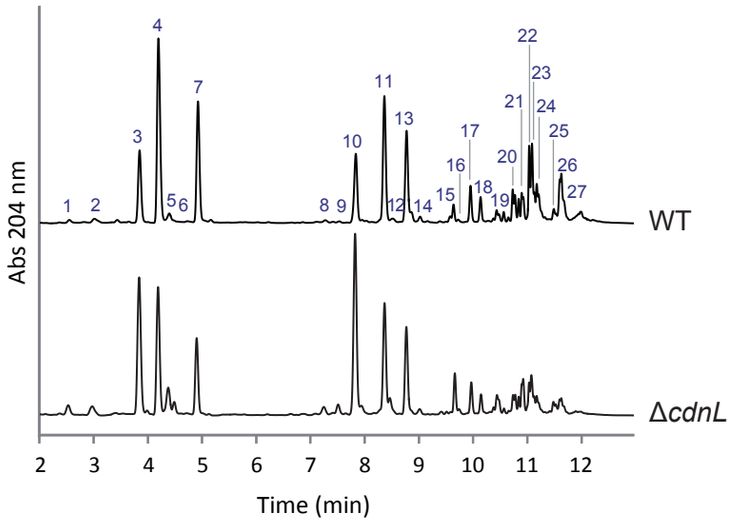

b.

Parameter	WT	Δ*cdnL*
Monomers	60.66	60.23
Dimers	26.23	32.22*
Trimers	13.10	7.55*
Crosslink	52.44	47.33
Anhydro	17.51	13.74*
Gly muropep.	21.66	43.54*
Pentapeptides	49.39	59.69*

c.

Peak	Muropeptide	Structure	WT	Δ*cdnL*
1	M3	GlcNAc-MurNAc-L-Ala-D-Glu-mDAP	0.60	1.41 *
2	M4^{G}	GlcNAc-MurNAc-L-Ala-D-Glu-mDAP-Gly	0.98	1.89 *
3	M5^{G}	GlcNAc-MurNAc-L-Ala-D-Glu-mDAP-D-Ala-Gly	10.69	20.39 *
4	M4	GlcNAc-MurNAc-L-Ala-D-Glu-mDAP-D-Ala	27.40	16.88 *
5	M2	GlcNAc-MurNAc-L-Ala-D-Glu	1.82	4.37 *
6	M44^{G}	M4-M4^{G} (DD-crosslink, dissaccharide lost)	0.00	1.54 *
7	M5	GlcNAc-MurNAc-L-Ala-D-Glu-mDAP-D-Ala-D-Ala	17.22	9.94 *
8	D44^{G}	M4-M4^{G} (DD-crosslink)	0.24	0.64 *
9	D43	M4-M3 (DD-crosslink)	0.16	0.75 *
10	D45^{G}	M4-M5^{G} (DD-crosslink)	5.18	12.50 *
11	D44	M4-M4 (DD-crosslink)	8.80	7.07 *
12	M5$^{G\ Anh}$	GlcNAc-(1-6anhydro)MurNAc-L-Ala-D-Glu-mDAP-D-Ala-Gly	0.75	2.37 *
13	D45	M4-M5 (DD-crosslink)	6.59	5.88
14	M4^{Anh}	GlcNAc-(1-6anhydro)MurNAc-L-Ala-D-Glu-mDAP-D-Ala	0.87	0.93
15	T445^{G}	M4-M4-M5^{G} (DD-crosslink)	0.63	1.35 *
16	M5^{Anh}	GlcNAc-(1-6anhydro)MurNAc-L-Ala-D-Glu-mDAP-D-Ala-D-Ala	0.33	0.51 *
17	T444	M4-M4-M4 (DD-crosslink)	1.27	0.98*
18	T445	M4-M4-M5 (DD-crosslink)	0.89	0.68 *
19	D45$^{G\ Anh}$	M4-M5$^{G\ Anh}$ (DD-crosslink)	0.92	1.57 *
20	D44^{Anh}	M4-M4^{Anh} (DD-crosslink)	2.41	1.57 *
21	D45^{Anh}	M4-M5^{Anh} (DD-crosslink)	1.93	2.25 *
22	T445$^{G\ Anh}$	M4-M4-M5$^{G\ Anh}$ (DD-crosslink)	1.77	0.73 *
23	T444^{Anh}	M4-M4-M4^{Anh} (DD-crosslink)	3.04	1.57 *
24	T445^{Anh}	M4-M4-M5^{Anh} (DD-crosslink)	1.99	0.76 *
25	T445$^{G\ Anh,\ Anh}$	M4-M4^{Anh}-M5$^{G\ Anh}$ (DD-crosslink)	0.50	0.57
26	T444$^{Anh,\ Anh}$	M4-M4^{Anh}-M4^{Anh} (DD-crosslink)	3.02	0.72 *
27	T445$^{Anh,\ Anh}$	M4-M4^{Anh}-M5^{Anh} (DD-crosslink)	0.00	0.20 *

Supplementary figure 2: Muropeptide composition is altered in ΔcdnL cells. a. Representative chromatograms of the muramidase-digested sacculi of WT and ΔcdnL cells. b. Relative molar abundance (%) of monomers, dimers, trimers, percentage of crosslinkage (proportion of cross-linked peptide side chains), muropeptides with a residue of (1-6 anhydro) N-acetyl muramic acid (Anhydro), Gly containing muropeptides (Gly muropep.), and pentapeptides. c. Muropeptide relative molar abundance (%). GlcNAc: N-Acetyl glucosamine. MurNAc: N-Acetyl muramic acid. Ala: Alanine. Glu: Glutamic acid. mDAP: meso-diaminopimelic acid. Gly: Glycine. Statistical analysis performed using t-test analysis. * = $P < 0.05$ and > 10% variation compared to WT.

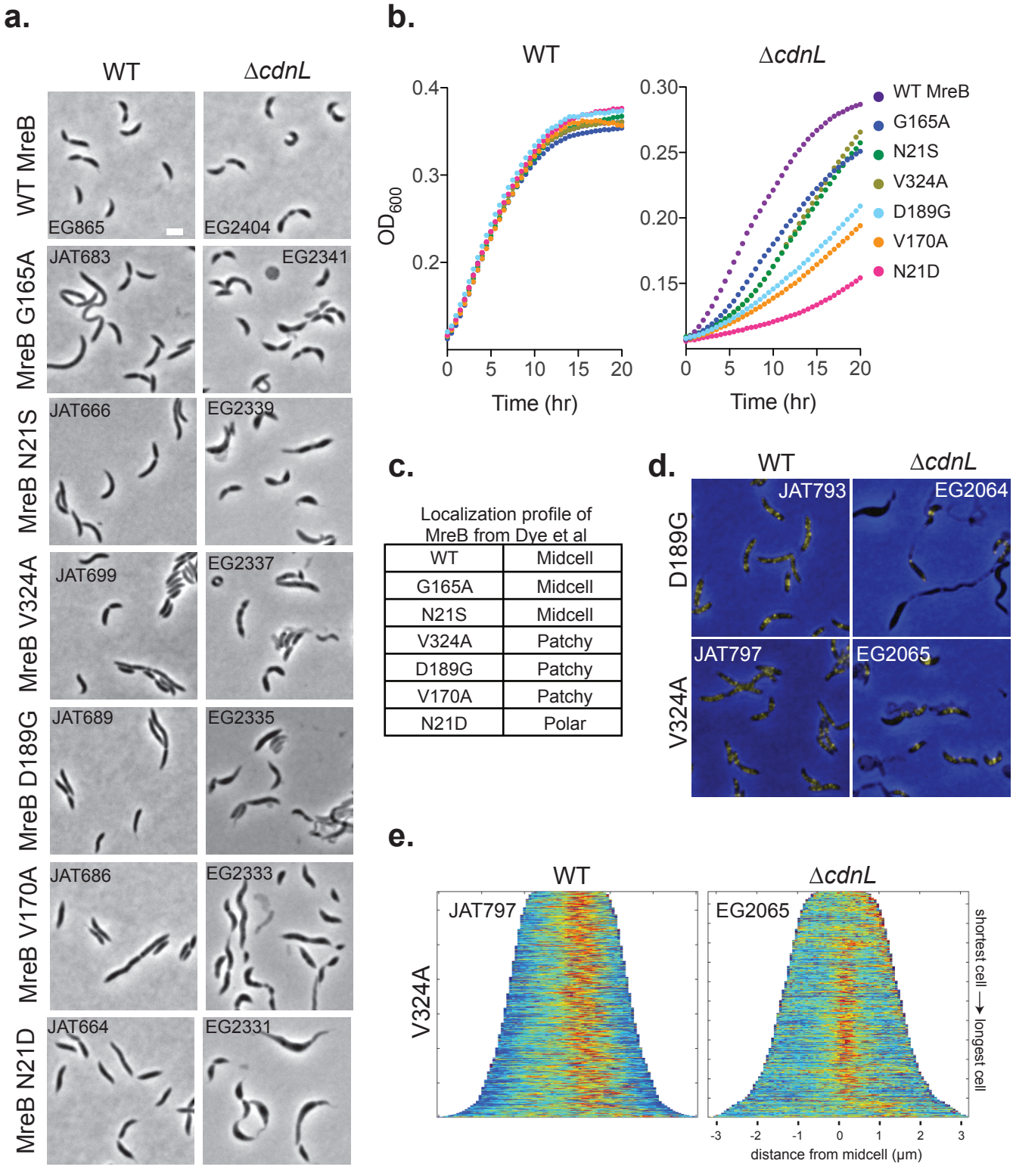

WT	Midcell
G165A	Midcell
N21S	Midcell
V324A	Patchy
D189G	Patchy
V170A	Patchy
N21D	Polar

Supplementary figure 3: mreB mutants are synthetic sick with ΔcdnL. a. Phase contrast images of WT and ΔcdnL cells expressing indicated mreB mutants at the mreB locus. Bar = 2 μm. b. Growth curves of strains shown in (a) grown in PYE. c. Summary of the localization of MreB mutants from Dye et al, 2011.27 d. Localization of indicated MreB mutants by expressing mutant version of venus-mreB from xylX locus. e. Demographs of MreB mutants shown in (d).

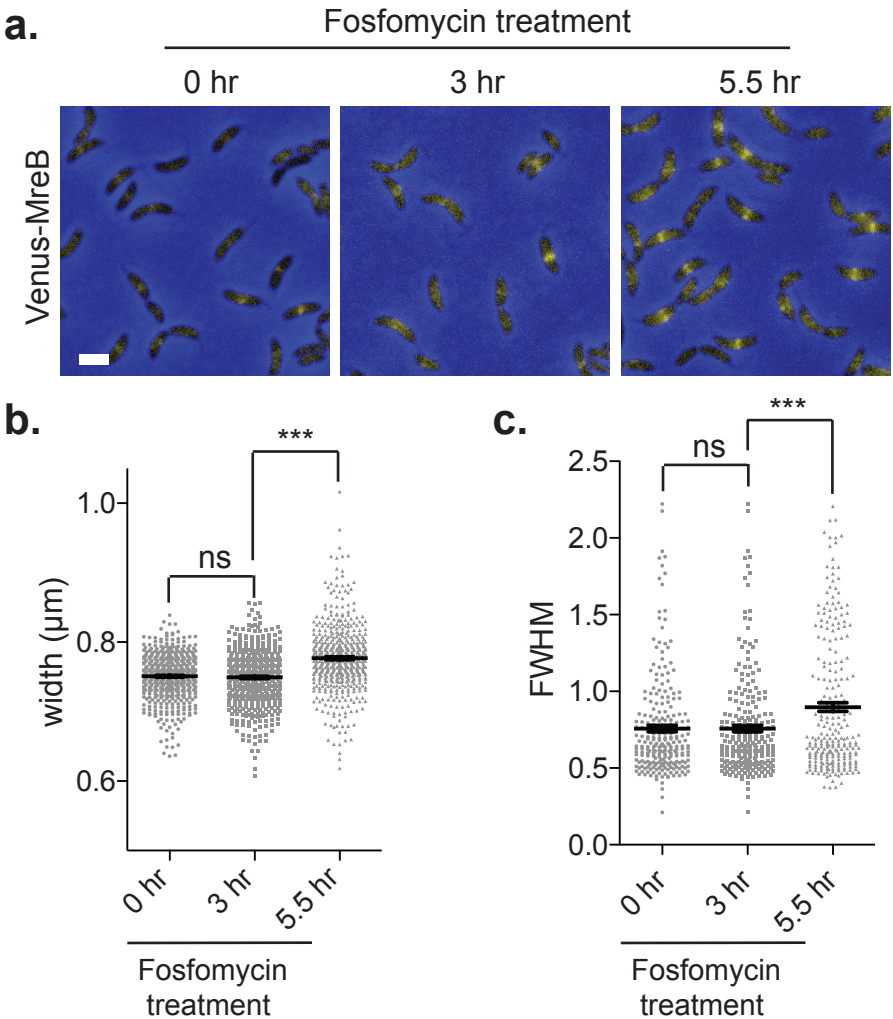

Supplementary figure 4: Depletion of lipid II by treating cells with fosfomycin causes an increase in cell width and FWHM of MreB localization. a. Merged images of cells expressing venus-mreB from the xylX promoter and treated with fosfomycin for indicated amount of time before imaging. Blue: phase contrast, yellow: Venus-MreB. Bar = 2 μm. b. Maximum cell width of cells shown in (a). n = 500 each, *** = P < 0.001, ns = not significant using one-way ANOVA with Bonferroni's Multiple Comparison Test. c. Full width at half maximum (FWHM) values of Venus-MreB in cells between 2.5 – 3 μm long and which have MreB localized at mid-cell. n = 245, *** = P < 0.001, ns = not significant using one-way ANOVA with Bonferroni's Multiple Comparison Test.

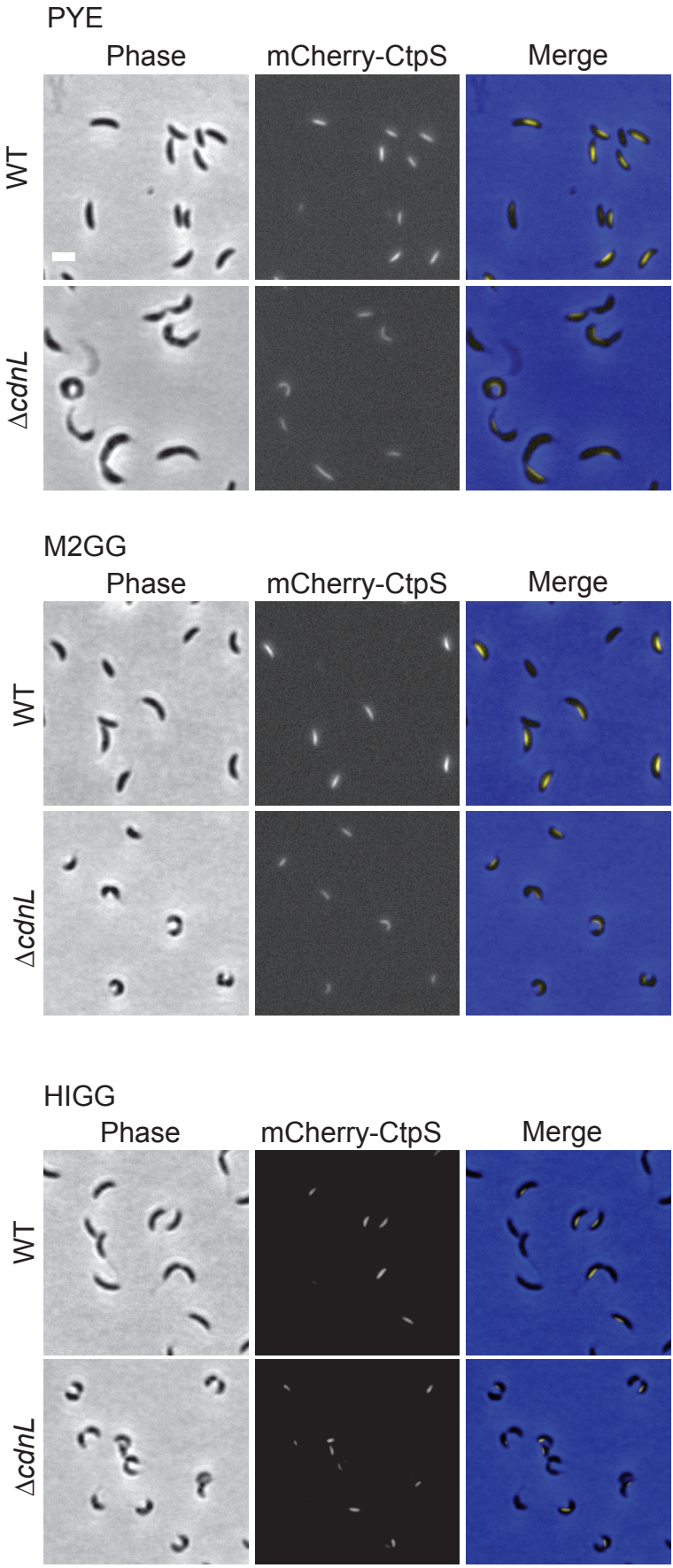

Supplementary figure 5. CTP synthase localization is weak in ΔcdnL cells compared to WT. Phase contrast, fluorescent and merged images of WT (EG1902) and ΔcdnL (EG1958) cells expressing mCherry – ctpS from the xylX locus grown in indicated media. Bar = 2 μm.